Author Manuscript

Author Manuscript

Author Manuscript

Author Manuscript

HHS Public Access

Author manuscript

Phys Med Biol. Author manuscript; available in PMC 2018 July 07.

Published in final edited form as:

Phys Med Biol. 2017 July 07; 62(13): R81–R123. doi:10.1088/1361-6560/aa6be8.

Magnetic Resonance Imaging with Hyperpolarized Agents: Methods and Applications

Erin B. Adamson[1], **Kai D. Ludwig**[1], **David G. Mummy**[3], and **Sean B. Fain**[1,2,3,*]

[1]Department of Medical Physics, University of Wisconsin – Madison, WI, U.S.A

[2]Department of Radiology, University of Wisconsin – Madison, WI, U.S.A

[3]Department of Biomedical Engineering, University of Wisconsin - Madison, WI, U.S.A

Abstract

In the past decade, hyperpolarized (HP) contrast agents have been under active development for MRI applications to address the twin challenges of functional and quantitative imaging. Both HP helium (^{3}He) and xenon (^{129}Xe) gases have reached the stage where they are under study in clinical research. HP ^{129}Xe, in particular, is poised for larger scale clinical research to investigate asthma, chronic obstructive pulmonary disease, and fibrotic lung diseases. With advances in polarizer technology and unique capabilities for imaging of ^{129}Xe gas exchange into lung tissue and blood, HP ^{129}Xe MRI is attracting new attention. In parallel, HP ^{13}C and ^{15}N MRI methods have steadily advanced in a wide range of pre-clinical research applications for imaging metabolism in various cancers and cardiac disease. The HP [1-^{13}C] pyruvate MRI technique, in particular, has undergone phase I trials in prostate cancer and is poised for investigational new drug trials at multiple institutions in cancer and cardiac applications. This review treats the methodology behind both HP gases and HP ^{13}C and ^{15}N liquid state agents. Gas and liquid phase HP agents share similar technologies for achieving non-equilibrium polarization outside the field of the MRI scanner, strategies for image data acquisition, and translational challenges in moving from pre-clinical to clinical research. To cover the wide array of methods and applications, this review is organized by numerical section into 1) a brief introduction, 2) the physical and biological properties of the most common polarized agents with a brief summary of applications and methods of polarization, 3) methods for image acquisition and reconstruction specific to improving data acquisition efficiency for HP MRI, 4) the main physical properties that enable unique measures of physiology or metabolic pathways, followed by a more detailed review of the literature describing the use of HP agents to study 5) metabolic pathways in cancer and cardiac disease and 6) lung function in both pre-clinical and clinical research studies, 7) some future directions and challenges, and 8) an overall summary.

1. Introduction

The field of magnetic resonance imaging (MRI) is experiencing continued expansion of contrast types and applications. One of the more active areas of research is the development

*Corresponding Author: Sean B. Fain, PhD, 1111 Highland Avenue, Room 1005, Madison, WI 53705-2275; Phone 608-262-2170; Fax 608-262-2413; sfain@wisc.edu.

Author Manuscript Author Manuscript Author Manuscript Author Manuscript

of hyperpolarized (HP) agents that include both gases and liquid state metabolites that are tailored for applications in the study of lung disease and *in vivo* metabolism. It is somewhat uncommon to have a single review encompass HP gases and HP ^{13}C and ^{15}N liquid state agents, although a limited number of such reviews do exist [1, 2]. This segregation of literature is partly because these fields have been historically divided into different research communities. Nonetheless, the two communities have recently been finding common ground in their efforts to translate their respective technologies to clinical settings. Both groups face similar regulatory challenges, employ techniques requiring dedicated broadband amplifier and receiver hardware, and benefit from advances in polarization technologies.

Section 2 of this review describes the physical and biological properties of the most common polarized agents with a focus on their utility for pre-clinical and clinical applications. The main focus is on the primary heteronuclei currently developed for translational applications, including ^{3}He, ^{129}Xe, and ^{13}C. The four primary physical techniques for achieving hyperpolarization are presented in the form of an overview, since excellent focused reviews of the underlying physics of these technologies already exist [3–6]. The relaxation properties of the main HP agents are presented, with an emphasis on the primary mechanisms that govern signal evolution and on acquisition strategies that lead to quantitative measurements of biological function.

Sections 3 and 4 focus on imaging acquisition and reconstruction approaches specific to HP MRI, including methods to improve data acquisition efficiency and exploit physical properties that enable unique measures of physiology or metabolic pathways. While longitudinal relaxation (T_1) properties limit data acquisition times to ~30–90 s for both HP ^{13}C metabolites and HP gases, transverse relaxation times (T_2) differ markedly for gas vs. injectable agents, leading to differing strategies for optimizing data acquisition efficiency. Non-equilibrium HP signal is irrevocably consumed with each radio-frequency (RF) excitation, accelerating polarization decay, and motivating the use and development of rapid k-space trajectories and more RF-efficient imaging techniques. Chemical shift imaging (CSI) methods are also important for both compartmental modeling of metabolic rates using HP ^{13}C MRI agents and for estimating gas exchange using HP ^{129}Xe gas MRI.

Sections 5 and 6 review the current literature on preclinical and clinical disease applications. Functional lung imaging via HP gas MRI is principally used to study lung diseases, both obstructive (e.g. asthma, chronic obstructive lung disease, and cystic fibrosis (CF)) and restrictive (e.g. interstitial lung disease (ILD) such as idiopathic pulmonary fibrosis (IPF) and radiation pneumonitis). HP ^{13}C-labeled agents are central to the study of metabolic pathway alterations in cancer *in vivo*, primarily sensing [1-^{13}C] pyruvate conversion to [1-^{13}C] lactate via upregulated glycolysis in breast, liver, and prostate cancer, but also for measuring oxidative stress due to coronary artery disease and inflammation.

Finally, sections 7 and 8 discuss future work and challenges to the field from the perspective of the authors. Some of the key remaining technical challenges to translation are improving overall polarization, improving signal-to-noise ratio (SNR) efficiency, reducing cost, and increasing T_1 time. The translational outlook is also discussed followed by an overall summary of this review.

Author Manuscript Author Manuscript Author Manuscript Author Manuscript

2. Physical and biological properties of polarized agents

The most common applications of HP agents use ^{3}He and ^{129}Xe gases and ^{13}C-labeled biomolecules. Typically, a 4–5 order of magnitude increase in polarization above thermal equilibrium is achieved by using physical methods of polarization. Polarization is combined with isotopic-enrichment of the nuclear magnetic resonance (NMR)-sensitive, non-hydrogen nuclei to further overcome the low density and natural abundance of these compounds *in vivo*. The advantage of investing effort to prepare such HP agents is that physiologic processes can be directly visualized *in vivo* (e.g. mapping gas distribution in the lungs or production of lactate from pyruvate in cancer) [7]. The achievable image SNR and spatial resolution of HP nuclei are governed largely by physical parameters such as the degree of polarization, gyromagnetic ratio, diffusion coefficient, T_1, and T_2 (Tables 1 & 2).

2.1. Methods of polarization

2.1.1. Spin exchange optical pumping (SEOP) & metastability exchange (ME)—There are two principal methods for polarizing gas agents: spin exchange optical pumping (SEOP) and metastability exchange (ME). ME is used only in ^{3}He applications, but SEOP is used for both ^{3}He and ^{129}Xe. Both methods depend on polarized laser light exciting a transition state of an electron spin followed by exchange of the resulting electronic polarization to the gas nucleus via the hyperfine interaction. The main difference between the two methods is that in SEOP the laser polarization interacts with an outer shell electron in an alkali metal (usually Rb), whereas in ME it interacts directly with the excited electron transition from the 2^3S_1 to 2^3P_0 state in the ^{3}He. This difference mainly influences the time required to reach the HP state.

The cross-section for hyperfine interactions between the Rb electron and the ^{3}He nuclei is small, so SEOP of ^{3}He is relatively inefficient, on the order of 15–20 hours for ~1 L of 40–50% polarized ^{3}He. The same volume of ^{3}He gas may be polarized to a level of 60–80% using ME in approximately 30–40 minutes [8].

SEOP of ^{129}Xe gas is more efficient than for ^{3}He, enabling faster polarization but also often employing active flow of a ^{129}Xe gas mixture during polarization, although this active flow is not strictly required [9]. Once polarized, the gas is captured via rapid deposition in a cold finger immersed in liquid nitrogen. Polarization levels may reach 40% at flow rates of 1 L per hour [10, 11]. Efficiency of polarization scales inversely with flow rate, necessitating longer collection times to achieve sufficient volumes for MRI studies. SEOP is used more commonly than ME due to its relative cost-effectiveness, simplicity, and robustness.

2.1.2. Dynamic nuclear polarization (DNP)—The dynamic nuclear polarization (DNP) technique transfers high spin polarization, usually from unpaired electrons, to NMR-active nuclei, thereby aligning their nuclear spins [12]. During a DNP experiment, a sample is doped with a stable, free electron radical [13] and cooled to cryogenic temperatures on the order of 1 K within a magnetic field where the electrons have a fractional polarization near unity. Continuous microwave irradiation near the electron paramagnetic resonance (EPR) frequency (ω_e) transfers the polarization from electrons to nuclei in the frozen matrix, increasing the nuclear polarization.

Author Manuscript Author Manuscript Author Manuscript Author Manuscript

Four continuous wave DNP mechanisms exist for polarizing liquids and solids: 1) the Overhauser effect, 2) the solid effect, 3) the cross effect, and 4) thermal mixing [14]. In frozen solutions or solids, polarization enhancement by microwave irradiation results from the solid effect and the thermal mixing mechanism. The dominating DNP mechanism depends on polarization conditions. When the EPR linewidth is narrower than the nuclear Larmor frequency (ω_n), the solid effect dominates and when the EPR linewidth is broader than the nuclear Larmor frequency, thermal mixing dominates [15]. Thermal mixing is the predominate mechanism at 3.35 T using Trityl radical [16]. Andenkjaer-Larsen and colleagues first showed that the enhanced solid-state nuclear polarization from DNP can be preserved after transitioning to the liquid state using a rapid dissolution system [3]. This development enabled molecular and metabolic processes to be probed in real time due to the longevity of the liquid state nuclear T_1 signal decay. The DNP method is widely used for polarizing biomolecules and other nuclei (typically ^{13}C, ^{15}N, and ^{1}H) for both imaging and/or spectroscopy applications.

2.1.3. Parahydrogen-induced polarization (PHIP) & signal amplification by reversible exchange (SABRE)—Parahydrogen-induced polarization (PHIP) and NMR signal amplification by reversible exchange (SABRE) are two alternative methods to DNP for hyperpolarizing liquid-state substrates. Both techniques rely on parahydrogen, the antisymmetric, highly spin-ordered state of hydrogen. Parahydrogen exhibits an overall spin angular momentum of zero and has 25% natural abundance at standard temperature and pressure. The other 75% of H_2 at standard temperature and pressure consists of orthohydrogen, the triply degenerate, symmetric spin state with overall spin angular momentum of one. In PHIP, enrichment of the parahydrogen state is accomplished by the combination of cooling H_2 molecules to cryogenic temperatures and using an appropriate paramagnetic material (e.g. activated carbon or iron oxide) to catalyze the forbidden transition from orthohydrogen to parahydrogen. At liquid nitrogen and liquid helium temperatures, this can lead to 50% and 100% parahydrogen enrichment, respectively. Transfer of this non-equilibrium polarization state to an appropriate heteronuclear spin system involves first performing a hydrogenation reaction with an appropriate catalyst. The catalysts used are commonly platinum group metals, which should be removed by filtering (e.g. by ion exchange) prior to *in vivo* injection. Spin order transfer to the ^{13}C-enriched precursor is then facilitated by either cycling the ambient magnetic field or via RF excitation. Magnetic cycling is most often used with a non-adiabatic decrease in field (~0.1 μT) that brings the spins into strong magnetic *J*-coupling to facilitate polarization exchange, followed by an adiabatic increase back to the Earth's magnetic field (~50 μT). RF excitation is designed to facilitate transfer of hyperpolarization to the heteronuclear spin system also via *J*-coupling and the nuclear Overhauser effect in which the spin symmetry of the H_2 molecule is broken [17]. An excellent review of the H_2 isomers and their role in PHIP is given by Duckett and Wood [18]. Several molecules have been successfully polarized using this method, most notably [1-^{13}C] succinate [19, 20]. Polarizations up to 50% have been achieved with PHIP [4, 19, 21, 22].

Like PHIP, SABRE uses parahydrogen as the source of spin order but, unlike PHIP, it does not require irreversible modification (i.e. direct hydrogenation) of the substrate. Instead,

Author Manuscript Author Manuscript Author Manuscript Author Manuscript

SABRE exploits reversible modification with lower catalyst concentrations (e.g. millimolar) and has been demonstrated using a pyridine substrate suitable for longer-lived T_1 relaxation times with ^{15}N-enriched precursors [23]. The newly emerging technique of SABRE-SHEATH (SABRE in SHield Enables Alignment Transfer to Heteronuclei) has further extended the potential of SABRE by achieving rapid and direct polarization of $^{15}N_2$-diazirine at low magnetic fields. This development highlights the potential for hour-long tracking of diazirine-containing molecules *in vitro* and *in vivo* by employing a relatively inexpensive polarization technique [24].

2.2. Commonly polarized agents

2.2.1. Overview of hyperpolarized gases—HP ^3He and ^{129}Xe gases are both used to investigate patterns of gas distribution, diffusion, and dynamic behavior in the lungs, and HP ^{129}Xe gas has also been used as a marker of brain perfusion.

^{3}He Gas: Low solubility and a high free diffusion coefficient make HP ^3He MRI a valuable method for exploring the lung air spaces using spin density imaging, and measuring microstructural dimensions via restricted diffusion weighting. However, global quantities of ^3He are limited, leading to high cost [25] and motivating migration to the more widely available ^{129}Xe nucleus [26].

^{129}Xe Gas: HP ^{129}Xe MRI typically uses a Xe gas mixture with the ^{129}Xe isotope enriched to ~85% from its natural abundance of 26%. The increased concentration of isotopically enriched ^{129}Xe helps to improve MR signal and compensate for the independent effects of a lower gyromagnetic ratio and reduced achievable hyperpolarization of ^{129}Xe relative to ^3He. All the major types of contrast-weighting demonstrated using ^3He MRI have now been replicated robustly with enriched ^{129}Xe [27, 28]. Unlike ^3He, ^{129}Xe diffuses from the gas phase into the tissues and blood, where chemical shifts associated with the local spin environment can be imaged directly to enable quantitative modeling of gas exchange [29–31]. More recently, the solubility of HP ^{129}Xe gas into the plasma and red blood cells has also been exploited for brain imaging, enabling characteristic measures of perfusion and T_1 relaxation in different brain compartments [32].

2.2.2. Overview of hyperpolarized metabolites—The physical properties of HP metabolites vary significantly for different molecular structures and ^{13}C or ^{15}N label locations within the molecule (Table 2). The most common ^{13}C-labeled agents include small molecules that play a central role in the major metabolic cycles in normal and diseased function. For a given metabolic pathway, the choice of metabolic substrate and the specific ^{13}C label site dictate the T_1 time and chemical shift of the metabolic tracer. In turn, the T_1 time influences the total acquisition time and SNR for imaging and spectroscopy. The chemical shift may further constrain acquisition parameters (e.g. echo time or RF excitation bandwidth) depending on the spectral bandwidth required to discriminate between different metabolic species. The physical properties of different metabolites enable the investigation of disease-related pathways, several of which are summarized below.

Author Manuscript Author Manuscript Author Manuscript Author Manuscript

Pyruvate: The most widely used and studied ^{13}C agent for HP MR is [1-^{13}C] pyruvic acid, due to a variety of advantageous properties. Pyruvic acid plays a central role in several metabolic pathways and is rapidly transported across the plasma membrane to the intracellular space. Its high solubility and self-glassing nature result in high solid-state polarization levels [33]. Further, [1-^{13}C] pyruvate has an extended T_1 time in the liquid state. [1-^{13}C] pyruvate undergoes cellular uptake via the monocarboxylate transporters [34] and its metabolism has been demonstrated *in vivo* as a means to probe the intracellular state of the tissues [35]. [1-^{13}C] pyruvate has been applied to investigate metabolic disorders, tumor response to therapy, cancer detection, cerebral dynamics and metabolism, pH, and more. Recently, the first in-human study using [1-^{13}C] pyruvic acid was conducted at the University of California San Francisco (NCT01229618) to investigate altered glycolysis in prostate cancer patients [36]. For a comprehensive list of [1-^{13}C] pyruvate applications, other existing reviews may be consulted by the reader [37–41].

Fumarate: HP fumarate has been developed as a sensitive marker for detecting cell death *in vivo* through conversion of [1,4-$^{13}C_2$] fumarate to [1,4-$^{13}C_2$] malate by the fumarase enzyme. Observations *in vitro* and in animal tumor models show a correlation between cellular membrane integrity and HP [1,4-$^{13}C_2$] malate signal [42, 43] originating from dying or necrotic cells with compromised membranes. Fumarate conversion to malate has also shown to be a sensitive marker of therapeutic response [44, 45] with increased amounts of malate signal detected prior to histological changes [46]. These results indicate that the observation of [1,4-$^{13}C_2$] fumarate conversion to [1,4-$^{13}C_2$] malate may provide a means of early disease response detection in addition to a direct measure of cell death and necrosis.

Dehydroascorbic acid (DHA) – ascorbic acid (AA) balance: Oxidative stress is associated with many cancers as well as numerous cardiovascular, neurological, and pulmonary diseases [47]. Vitamin C, also known as ascorbic acid (AA), plays an important role in regulating intracellular reactive oxygen species concentrations to maintain the reduction/oxidation (redox) state of a cell. Dehydroascorbic acid (DHA), the oxidized form of AA, was developed as an investigative probe to measure chemical reduction potential. An increased amount of [1-^{13}C] DHA reduction to [1-^{13}C] AA *in vivo* was found to correlate with increased intracellular antioxidant concentrations in a diabetic mouse model [48], indicating HP [1-^{13}C] DHA reduction may assess the altered redox capacity in disease and may also hold the potential to monitor treatment response. The long T_1's observed for [1-^{13}C] DHA (56 s) are favorable for clinical field strengths but [1-^{13}C] DHA still suffers from low overall liquid-state polarization (~6%). Additionally, DHA can rapidly hydrolyze and dehydrate upon dissolution [49], resulting in a complex ^{13}C NMR spectrum and limiting its availability. To date, [1-^{13}C] DHA is the only endogenous molecular MRI probe able to investigate the intracellular redox state.

Bicarbonate: Many disease states, including cancer, infection, inflammation, heart disease, and arthritis are associated with a pH imbalance [50]. Bicarbonate is the primary endogenous, extracellular buffer for acid-base regulation within the body through interconversion with carbon dioxide catalyzed by the carbonic anhydrase enzyme. The potential to determine HP ^{13}C bicarbonate and ^{13}C carbon dioxide spatial distributions and

Author Manuscript Author Manuscript Author Manuscript Author Manuscript

to measure extracellular pH has been demonstrated in murine tumors [51]. However, these techniques may overestimate pH due to the slow equilibration of the ^{13}C label [52]. Prolonged imaging periods are limited by the short T_1's observed with HP ^{13}C bicarbonate (10.1 s) and ^{13}C carbon dioxide (9.8 s) [51]. Several other DNP probes have been investigated to measure pH including ^{13}C-labeled α-ketoisocaproate [53], [1-^{13}C] pyruvate [54], ^{13}C,^{15}N *N*-(2-acetamido)-2-aminoethanesulfonic acid [55], ^{15}N pyridine [56], and ^{89}Y complex [57], among others.

Other agents: Additional ^{13}C MR agents that have been investigated include ^{13}C-enriched urea, glutamine, glucose, lactate, fructose, and glutamate, among others. These agents and their applications are well reviewed elsewhere [38, 58].

2.3. Physical properties of polarized agents

2.3.1. Spin-lattice exchange (T_1) behavior—Most HP nuclei possess comparatively long T_1 relaxation times relative to ^{1}H nuclei, due in part to their lower nuclear gyromagnetic ratio (γ), (e.g. ~4x lower for ^{129}Xe and ^{13}C). While long T_1 relaxation times may be problematic for conventional analytical NMR studies, the opposite is true for HP nuclei. The HP decay back to thermal equilibrium is caused, in part, by T_1 relaxation, which therefore determines the time window available for imaging. Hence, very high magnetic field strengths are not advantageous for the study of HP agents due to T_1 shortening. An example of the transient decay of metabolic signals in dynamic HP ^{13}C spectra is displayed in Figure 1, where the rate of decay for each metabolite is determined by its characteristic T_1 relaxation time, the RF excitation signal consumption, and the rate of metabolic conversion.

The general mechanisms for polarized spin T_1 relaxation are the same as for conventional thermal polarization. Polarized energy is transferred to the "lattice" of the local molecular environment. This transfer originates from both intrinsic and extrinsic factors such that

$$R_{1,obs}=\frac{1}{T_{1,obs}}=\frac{1}{T_{1,intrinsic}}+\frac{1}{T_{1,extrinsic}} \quad (1)$$

where $R_{1,obs}$ is the observed relaxation rate and $T_{1,obs}$ is the measured relaxation time. Typical intrinsic relaxation mechanisms include inter- or intra-molecular interactions such as dipole-dipole, spin-rotation, and van der Waals interactions. Typical extrinsic factors include interactions with external paramagnetic nuclei and diffusive motion in the presence of field inhomogeneity.

2.3.1.1. Paramagnetic effects in HP gas nuclei: Different T_1 relaxation mechanisms dominate depending on the chemical nature and mixture of the HP nucleus of interest. ^{3}He gas is inert with limited solubility such that, in a pure gas mixture, dipole-dipole exchange with other ^{3}He gas nuclei is the dominant mechanism of relaxation [59, 60]. A T_1 time in the range of 100 h in a small holding field (e.g. ~1 mT) is achievable, making it is feasible to ship HP ^{3}He gases from a central location to sites without polarizers [61]. The situation is different for ^{129}Xe gas because both spin-rotation and van der Waals interactions dominate

Author Manuscript Author Manuscript Author Manuscript Author Manuscript

over dipole-dipole interactions due to short-lived chemical (electron cloud) associations to form ^{129}Xe molecules. The dominant contribution from van der Waals interactions reduces observed T_1 times for pure Xe gas to approximately 4.5 hours in a holding field [60].

When either of the HP gases are mixed with air, the most relevant extrinsic relaxation mechanism is the interaction with paramagnetic oxygen. SEOP and storage of HP gases therefore takes place in vessels purged of oxygen. As mentioned above, SEOP is performed under constant flow resulting in a xenon ice that is sublimated back to a gas prior to delivery to the patient. For pulmonary MRI, the HP gas is delivered to the subject as an anoxic gas mixture of ^{3}He or ^{129}Xe and nitrogen. Once inhaled into the lungs, the observed relaxation rate depends on extrinsic contribution from partial pressure of oxygen (pO_2) residual in the lungs [62, 63]:

$$\mathrm{T}_{1,\mathrm{O}_2}=0.388\cdot\frac{\mathrm{pO}_2[\mathrm{bar}]}{1.0135}\frac{273\,\mathrm{K}}{\mathrm{T}}\approx\frac{\mathrm{pO}_2}{\xi},\quad \xi=2.61\,\mathrm{bar}\cdot\mathrm{s} \tag{2}$$

here calculated at body temperature (T = 310.15 K). Once the dose mixes with residual oxygen in the lungs, T_1 is reduced to approximately 30 s, but signal is sustained over the time of a typical breath-hold.

In contrast to lung imaging, HP ^{129}Xe signal in the brain is improved by delivering the gas mixture (or “dose”) with a non-negligible oxygen concentration. The ideal fraction of oxygen in the dose balances the expected concentration of paramagnetic oxygen in the lungs with that of oxyhemoglobin in the blood, which mitigates T_1 shortening of dissolved ^{129}Xe. Experiments in rats suggest an optimal pulmonary oxygen concentration of 25–35% to maximize HP ^{129}Xe signal in the brain [64].

2.3.1.2. Paramagnetic effects in spin-labeled molecules: The situation is more complicated for ^{13}C and ^{15}N MRI due to the more varied local chemical environment within the molecular structures of labeled metabolites and compounds. The observed relaxation rate ($R_{1,obs}$) of the ^{13}C nucleus is a sum of four different rates – dipole-dipole ($R_{1,dd}$), scalar ($R_{1,sc}$), spin rotation ($R_{1,sr}$), and chemical shift anisotropy ($R_{1,csa}$):

$$R_{1,obs}=R_{1,dd}+R_{1,sc}+R_{1,sr}+R_{1,csa} \tag{3}$$

The dominant decay mechanism remains dipole-dipole interactions, but the probability for these interactions varies with location in the molecule. Nearby intramolecular nuclei with net magnetic moments can induce relaxation in the polarized carbon, destroying the polarization enhancement. For protonated carbons, the dipole-dipole relaxation rate dominates, leading to short relaxation times [65]. The relaxation rate is given by [66]:

$$R_{1,dd}=\hbar^2\gamma_H^2\gamma_C^2\tau_R\sum_j r_j^{-6} \tag{4}$$

Author Manuscript Author Manuscript Author Manuscript Author Manuscript

where r_j is the distance between the carbon and the j^{th} hydrogen and τ_R is the correlation time. This relaxation rate is proportional to the square of the gyromagnetic ratios of the bound nuclei, making coupling of ^{13}C nuclei with high γ nuclei, such as ^{1}H, undesirable. In molecules with quaternary carbons, dipole-dipole relaxation is minimal. In these instances, the three other relaxation mechanisms - scalar relaxation, chemical shift anisotropy, and spin rotation - can significantly influence the relaxation rate of carbon [67]. Carboxylic acid carbons, as well as other non-protonated carbons thus exhibit longer T_1 relaxation times. This can be attributed to their increased distance from non-zero spin nuclei. The consequence of the local chemical environment on relaxation rates can be seen when looking at glucose (Table 2) [58, 68–71] or acetaminophen (Figure 2).

2.3.2. Spin-spin (T_2 and T_2*) behavior—Spin-spin exchange is dominated in both HP ^{13}C and gas applications by local field inhomogeneities. This is especially true in the lungs, where anatomic heterogeneity (i.e. air-tissue boundaries) causes an extremely short T_2* of 1–2 ms for proton signal in the tissue [72]. HP gases filling the airspaces have somewhat longer T_2* times of 10–20 ms [73]. The very short T_2* experienced by proton spins extends to HP ^{129}Xe MRI dissolved in the tissue and blood, and therefore, measures of gas exchange using spectroscopic imaging of HP ^{129}Xe are complicated by mismatch in T_2* decay between dissolved and gaseous phases and the large chemical shift between them (Figure 3) [31].

By contrast *in vivo* HP ^{13}C metabolites have substantially larger T_2* than gases in the lungs, anecdotally measured to be on the order of 40 ms *in vivo* [74], while T_2 ranges from 0.1–5 s [75]. As with ^{129}Xe, it is not entirely clear that metabolites within the vascular vs. intracellular spaces share the same decay rates, with potential consequences for modeling metabolic rates of conversion such as the conversion of pyruvate to lactate in cancer [76].

2.3.3. Diffusion and solubility properties—The physical diffusion and solubility properties differ markedly for HP ^{3}He and ^{129}Xe (Table 1) which impacts applications for the two gases. The high free diffusion coefficient of HP ^{3}He enables measurement of displacements on the order of alveolar diameters (a few hundred micrometers) or greater [73, 77]. Equivalent measurements on HP ^{129}Xe [28] are also possible, but more challenging due to its lower free diffusivity and T_2* decay for longer echo times.

Unlike HP ^{3}He, HP ^{129}Xe is also relatively soluble in blood and tissue (Table 1), where it reflects useful properties of the local spin environment. Thus, image contrast in ^{129}Xe represents a combination of ventilation, tissue density, blood volume, and perfusion that can be resolved through CSI, providing opportunities for differentiating between separate compartments of HP ^{129}Xe gas exchange.

Similar to HP ^{129}Xe, HP metabolites may access different biological compartments, namely intra- and extra-cellular spaces, where they exhibit unique diffusion properties (Table 2). [78] As a result, diffusion weighted imaging (DWI) can be used to differentiate between intra- and extra-cellular HP metabolites, giving further insight into the metabolic processes and cellular transporters at play.

Author Manuscript Author Manuscript Author Manuscript Author Manuscript

3. Imaging Strategies

3.1. Effect of flip angle on temporal kinetics

In most imaging settings, the global flip angle is known and can be used to correct for RF consumption of HP signal based on the number and sequence of applied RF pulses. However, regional variations in RF power transmission can be problematic, often requiring either estimation or direct measurement of the transmit field. This is most commonly a factor for HP gas imaging, since the field must be known or at least approximated over a field of view encompassing the entire lung volume. Even after controlling for known factors, dynamic processes are further complicated by physiological phenomena, such as local variations in perfusion or pO_2, that can confound observed rates of metabolism or gas flow. In such cases, independent measurements of local flip angle [79] or perfusion [80] are required to achieve quantitative measures.

3.2. Improving data acquisition efficiency

3.2.1. Fast imaging trajectories—The most appropriate acquisition for a given study is determined by balancing tradeoffs between SNR, spatial resolution, temporal resolution, RF efficiency, and reconstruction efficiency in order to best meet imaging goals and requirements. Due to the continuous decay of the HP spins back to thermal equilibrium, imaging of HP gases and HP ^{13}C substrates requires acquisition schemes that rapidly traverse k-space in an RF-efficient manner [81]. While many of the same imaging trajectories have been used for both HP gas and HP ^{13}C imaging, short echo time, radial spoiled gradient echo imaging is particularly well suited to the short T_2^* of HP ^{3}He and ^{129}Xe, and is often used for HP gas imaging. The short echo time of radial imaging makes it robust against field heterogeneities in the lung while the inherent oversampling of the center of k-space results in a sequence that is robust against motion artifacts and well-suited to dynamic imaging. Moreover, it is possible to perform angular undersampling in conjunction with radial oversampling to expedite the image acquisition without a significant loss in spatial resolution or image contrast [82]. Improvements in acquisition time are particularly important for HP gas imaging because it is performed during a breath-hold. This physiologic window on acquisition time has spurred interest in compressed sensing techniques to enable higher resolution or 3D imaging, as well as to facilitate multiple diffusion-weighted acquisitions [83]. Parallel imaging has also been employed to leverage the HP gas signal stability that is unique to non-equilibrium HP spins, with higher or similar image SNR achievable with fewer acquisitions, enabling improvements in both temporal and spatial resolution. [84]

Two main k-space trajectories have been proposed for fast HP imaging of ^{13}C substrates: echo planar imaging (EPI) [85–91] and spiral imaging [74, 92–94], although other rapid imaging techniques such as radial sampling [95] and concentric rings trajectories [96] have been employed. Additionally, compressed sensing techniques have been employed to increase image acquisition speed [88–90, 97].

EPI is an RF-efficient gradient echo acquisition that rapidly fills k-space in as little as a single excitation. [98]. However, the non-centric encoding scheme, inherent to single-shot

Author Manuscript Author Manuscript Author Manuscript Author Manuscript

EPI, limits the achievable image contrast, which is undesirable when dealing with limited HP signal. Multi-shot EPI, can be used to begin encoding at the center of k-space, thereby boosting image SNR at the cost of reduced RF efficiency [91, 99]. For EPI trajectories, HP ^{13}C SNR is also improved by matching the readout duration to the long transverse decay time, with the penalty of increased image blurring from T_2* decay. SNR may also be degraded by non-uniform k-space sampling [81]. To counteract deleterious SNR effects, the use of balanced steady state free precession EPI has been advocated to preserve transverse magnetization [100, 101]. If acquisition speed for dynamic metabolic imaging is desired over maximizing SNR, the field of view can be easily reduced in one or more directions for EPI readouts, allowing faster data collection [102]. Additionally, EPI readouts have the advantage over non-Cartesian acquisitions in that they can readily incorporate parallel imaging and compressed sensing techniques to further increase image SNR or temporal acquisition efficiency [89, 90, 97, 102, 103].

Spiral imaging is another RF efficient acquisition scheme that can fill k-space with a single excitation. [98, 102, 104]. Spiral imaging readouts provide improved temporal sampling efficiency over EPI readouts since the corners of k-space are not acquired, making them attractive for imaging HP metabolites with short T_1 (Table 2) or for rapid, dynamic HP imaging. Spiral sampling also starts at the center of k-space, unlike EPI, eliminating the need to perform multi-shot imaging to maximize image contrast. A significant drawback to spiral imaging is that chemical shift phase errors manifest as image blurring, limiting the achievable spatial resolution [81, 102]. This is of particular concern for HP ^{13}C imaging with sparse spectra, where chemical shifts may be up to ~10's of ppm, and requires dedicated spectral separation techniques to resolve. Like EPI, SNR can be improved by matching the spiral readout duration to the expected T_2* decay time at the cost of image sharpness. However, spiral readouts do not present the flexibility to increase acquisition efficiency by adjusting the field of view like EPI because the sampling resolution is limited by gradient performance and duration. Furthermore, this non-Cartesian acquisition does not easily lend itself to acceleration techniques such as parallel imaging and compressed sensing methods that are advantageous for fast, under-sampled imaging with HP agents [102].

3.2.2. Strategies for robust multi-spectral imaging—HP imaging is not only complicated by its inherent dependence on nuclear spins in thermal non-equilibrium, but also, in the case of ^{13}C and ^{129}Xe, by the presence of unique spectral components. Such multi-spectral data induces chemical shift artifacts and hinders accurate quantification of physiologic processes if left unaccounted for [92]. To date, three major multi-spectral imaging techniques for chemical species isolation have been translated from conventional ^{1}H imaging to HP imaging: chemical shift imaging (CSI) [32, 81, 91, 92], modeling of HP spectra similar to iterative decomposition of water and fat with echo asymmetry and least-squares estimation (IDEAL) methods [31, 74, 81, 93, 101, 105–108], and the use of spectral-spatial (SPSP) excitation [86, 109–111].

A fundamental trait of all CSI techniques is acquisition of spectral data in addition to spatial information. The most basic form of CSI employs multiple RF excitations, followed by a single phase-encode step and collection of a free induction decay to fill points in k-space. However, this RF-inefficiency is unsuitable for dynamic HP imaging. Free induction decay

Author Manuscript Author Manuscript Author Manuscript Author Manuscript

CSI is also prone to Gibbs ringing artifacts due to non-uniformly distributed HP signal in k-space. However, the absence of a readout gradient makes this technique robust against both gradient errors and motion or flow artifacts. Additionally, the acquisition of a full spectrum renders this technique stable against off-resonance artifacts [81]. Alternative k-space trajectories that do employ readout gradients can be used to sample k-space more quickly, and with increased RF efficiency. Echo planar spectroscopic imaging and spiral CSI both sample a portion of k-space repeatedly to gain spectral information following an RF excitation. The spectral bandwidth of the acquisition is determined by the time taken to return to a given point in k-space. Therefore, temporal, spatial, and spectral resolutions are all limited by the maximum amplitude and slew rates of the gradient hardware [81, 91, 92].

The second method of multi-spectral imaging relies on modeling of the HP spectra, analogous to the IDEAL reconstruction formalism. This technique involves acquiring data at multiple, pre-determined echo times that produce different phase offsets between the unique spectral components. Iterative reconstruction with least-squares minimization is then used to isolate the different chemical species [74, 81, 105, 107]. A minimum of n+1 echoes must be acquired to separate n species, which may allow for shorter scan times than other CSI techniques. This IDEAL concept has been further accelerated by k-t spiral imaging, which oversamples k-space and uses the phase evolution between spiral turns to extract spectral data [93]. The downside to these IDEAL-based techniques is that they rely on prior knowledge of the spectra. As a result, slice-selective free induction decays are often collected between time points in dynamic studies to guide the IDEAL reconstruction [112].

The third technique for multi-spectral imaging is SPSP excitation, in which a train of RF subpulses, modulated by a Gaussian-like envelope, are played out in conjunction with an oscillating slice-select gradient to excite a narrow band of frequencies in a given slice [86, 109, 110, 113, 114]. The subpulse spacing determines the spectral stopband while the modulating envelope governs the spectral passband. SPSP pulses are especially useful for HP ^{13}C imaging since each metabolite can be excited independently with different flip angles [86, 110, 111, 115, 116]. Low concentration metabolites can be excited with high flip angles to increase their SNR, while higher-SNR injected substrates can be excited with lower flip angles to preserve HP signal. Alternatively, SPSP pulses can be designed to excite all desired species simultaneously with different flip angles at the cost of requiring another form of spectroscopic imaging for species differentiation [90, 111, 116]. A large benefit of SPSP excitation is the elimination of chemical shift effects when only a single species is excited. However, SPSP pulses are often long (e.g., ~10's of ms) in order to excite a narrow passband, and they rely on prior knowledge of the spectrum being sampled in order to excite the correct frequency. Another drawback of this technique is that gradient amplitude and slew rate limitations restrict the achievable slice thickness due to the oscillating gradient used for slice-selection [110, 113, 114].

4. Deriving functional measures from hyperpolarized agents

4.1. Ventilation weighted imaging of gas distribution in the lungs

Spin density images acquired during a breath-hold represent a snapshot of the distribution of HP gas within the lungs. The resulting "ventilation defects" (Figure 4) are influenced by

Author Manuscript Author Manuscript Author Manuscript Author Manuscript

regional airway obstruction and air trapping. [117, 118] The ventilation defect volume [117, 119, 120], ventilated volume [119, 121], and coefficient of variation [122, 123] derived from these images have all proven useful for demonstrating regional heterogeneity of ventilation in a wide range of obstructive lung diseases. Measures of ventilation defects are also sensitive to subclinical decline in function due to aging in healthy never-smokers [118, 123] and in smokers [124–126].

The ventilation defect percentage (VDP) is an emerging biomarker defined as the defected lung volume normalized by the total lung volume [127–130], where total lung volume is typically acquired from a proton image of the lungs during a separate breath-hold. Inadequate registration between the two breath-holds may add systematic error to the ventilation defect measurement. Recently, acquiring both HP gas and proton images of the total lung volume within the same breath-hold was demonstrated to improve spatial registration [131]. Multiple groups have demonstrated repeatability [120, 129, 132, 133] and validity of the VDP measure in comparison to pulmonary function testing [120, 123, 134–136] and as a biomarker of severity of lung disease [123, 134, 136]. Overall larger values for VDP are observed after inhalation of ^{129}Xe vs. ^{3}He in the same individual [137], a bias which is likely attributable to the difference in gas densities (Table 1), although this remains a matter for speculation and further research [138].

4.2. pO_2 measurement: modeling T_1 decay

As discussed in the context of SEOP, the paramagnetic effects of oxygen reduce the T_1 and T_2 of HP gases [139] and can be exploited to provide a quantitative estimate of regional pO_2 [63, 140, 141]. Typically, the same slice is imaged repeatedly at different delay times following gas inhalation to isolate signal loss due to local O_2 concentration from signal decay due to the excitation flip angle [142]. Each measurement is performed within a single breath-hold [79, 141], and modified centric and reverse-centric view orders mitigate effects due to regionally variable flip angle (B_1-field variation) [79]. Gas flow effects within the lungs during a breath-hold have recently been characterized using ^{3}He, underscoring that this method of pO_2 measurement reflects both regional pO_2 and local patterns of ventilation and flow [143]. Regional pO_2 measures can potentially be used to calculate the ratio of ventilation-to-perfusion [142], and pO_2 measurements have recently been used as a marker of disease severity in a study of ventilation-to-perfusion ratio heterogeneity in smokers [144, 145].

4.3. Spectroscopic MRI

4.3.1. Modeling of gas exchange using ^{129}Xe MRI—The soluble “dissolved phase” fraction of ^{129}Xe in blood and tissues is approximately 2% of the total signal. Polarized gas nuclei diffuse rapidly between gas, blood cells, and plasma/tissue compartments, with chemical shifts of 0, 222, and 198 ppm respectively (Figure 3) [146]. The chemical-shift between ^{129}Xe in the differing local chemical environments, associated with the dissolved tissue and red blood cell (RBC) vs. gas compartments, can be resolved by a combination of SPSP excitation and Dixon methods that use phase to separately reconstruct dissolved tissue and RBC compartments [147]. The similarity of this problem to quantitative fat-water separation in conventional ^{1}H MRI (i.e. IDEAL) led to the introduction of least-square

Author Manuscript Author Manuscript Author Manuscript Author Manuscript

modeling of the known spectral shifts using multi-echo acquisitions [31]. However, the short T_2* of the dissolved phase components still pose a challenge to quantitative measures.

Compartmental modeling of these components has advanced relatively rapidly [148]. Simple and robust single voxel MR spectroscopy readily resolves tissue and blood fractions and enables the calculation of the blood-to-tissue ratio as a possible biomarker of "diffusion block" [149, 150]. Quantitative measures such as "saturation transfer time" allow the kinetics of ^{129}Xe recovery to be modeled. These more advanced methods can provide direct [29–31, 151] or indirect [147, 152] estimates of average septal wall thickness and alveolar surface area-to-volume ratio [147, 148, 153]. Both single-voxel [153, 154] and spectroscopic imaging methods [30, 31] are feasible.

4.3.2. Modeling of pyruvate-to-lactate conversion rates—Due to both the amenability of [1-^{13}C] pyruvate to polarization and its important role in energy metabolism, several semi-quantitative approaches have been developed to characterize the pyruvate-to-lactate conversion with HP magnetic resonance spectroscopy (MRS) and magnetic resonance spectroscopic imaging (MRSI). Simplified ratio methods, such as lactate-to-pyruvate ratios, have been employed for single or averaged time points to assess relative metabolite concentrations [155]. More advanced modeling methods were introduced by Day *et al.* incorporating a two-compartment exchange model for time-resolved data that accounts for bidirectional rates of conversion from pyruvate to lactate [76]. More recently, area-under-the-curve ratios were introduced for dynamic acquisitions that simplify measurements while still utilizing the entire pyruvate and lactate kinetic data [156]. The area-under-the-curve ratios are proportional to rate constants derived from two-compartment exchange models, but are thought to be more robust to motion or noise as they do not depend on fitting a model to the data.

Robust models of physiological rate-limiting steps, such as delivery of the injected substrate via perfusion, and the impact of vascular and extra-vascular tissue volumes not accessible for metabolic conversion, are still in development [78, 157–161].

4.4. Diffusion weighted imaging (DWI)

4.4.1. Using high gas diffusion to measure lung microstructure—DWI exploits the high free diffusion of ^{3}He and ^{129}Xe gases, allowing indirect measurement of the average dimensions of the lung airspaces and microstructure. When ^{3}He or ^{129}Xe gas is restricted by tissue boundaries, the diffusivity measurement is referred to as the apparent diffusion coefficient (ADC). ADC is regarded as a surrogate for localized airway or acinar dimensions, and can be calculated for each voxel to construct a semi-quantitative ADC map (Figure 5). Regional ADC changes have been observed in response to increases in lung volume [162, 163], gravity dependence [162, 164, 165], age [166], and emphysema in chronic obstructive pulmonary disease (COPD) or α-1-antitrypsin deficiency [121, 164, 167, 168]. ADC values for ^{129}Xe are lower than those of ^{3}He by an order of magnitude due to the higher density of ^{129}Xe gas (Table 1). Despite this difference in magnitude, ^{129}Xe ADC values in human subjects are also strongly associated with increased COPD severity and correlate well with ^{3}He ADC values [27, 138, 165].

Author Manuscript Author Manuscript Author Manuscript Author Manuscript

5. Applications of hyperpolarized ^{13}C MRI to pre-clinical and clinical research

5.1. Pre-clinical studies

5.1.1. Prostate cancer ^{13}C MRI—The prevalence of prostate cancer (over 180,000 new diagnoses expected in 2016 in the United States alone) has spurred research investigating non-invasive, molecular imaging techniques that could guide treatment decisions and improve treatment monitoring [169]. Investigation into HP ^{13}C MRI applications in breast and prostate cancer, have been largely fueled by the desire to exploit the Warburg effect and have shown promising results in pre-clinical studies. HP [1-^{13}C] pyruvate is a particularly compelling candidate to probe upregulation of aerobic glycolysis exhibited in cancerous tumors [170]. One of the earliest *in vivo* applications of HP ^{13}C MRSI was performed in a transgenic adenocarcinoma of mouse prostate (TRAMP) model. This study highlighted the promise of HP [1-^{13}C] pyruvate MRSI to differentiate malignant and benign tissues through the observation of elevated lactate levels in prostate tumors over normal prostate glands [171]. A correlation between lactate level and tumor histologic grade has since been demonstrated, as well as increased spatial heterogeneity of lactate with more advanced tumors [170, 172]. Additionally, HP substrates, including ^{13}C bicarbonate, ^{13}C DHA, and [2-^{13}C] fructose, have been used to measure tumor pH, redox potential, and metabolism, respectively, in TRAMP models [173–175].

5.1.2. Breast cancer ^{13}C MRI—HP [1-^{13}C] pyruvate has been used to test the degree of aerobic glycolysis vs. tumor progression in breast cancer cell xenografts in mice, with higher conversion rates observed for more indolent xenografts [176, 177]. Several studies have also looked at biologic factors modulating the observed metabolic signals in breast cancer studies, including perfusion [178], cellular transport [179], and endogenous lactate and lactate dehydrogenase (LDH) concentrations [180]. Both perfusion and cellular expression of monocarboxylate transporters were important factors affecting the observed metabolic signals. This work has been extended to study the impact of inhibiting key enzymes implicated in cancer development on the observed HP metabolite levels (e.g., phosphatidylinositol-e-kinase (PI3K) which modulates LDH activity). Ward *et al.* observed a significant drop in lactate levels following PI3K inhibition, demonstrating the sensitivity of HP ^{13}C MRS to LDH activity modulated by PI3K [181]. The possibility of treatment monitoring of breast cancer using HP [1-^{13}C] pyruvate has also been investigated. Butt *et al.* used an estrogen-dependent, murine breast cancer model, exhibiting an angiogenic switch in its transition from primary to malignant cancer, to study the effects of tamoxifen on the apparent conversion rate of pyruvate-to-lactate. They observed a significant increase in the apparent conversion rate during the malignant transition in untreated mice, while the tamoxifen treated group saw the same trend but without statistical significance (Figure 6) [182]. This range of preclinical work lends additional insight into the biochemical and physiologic processes associated with breast cancer pathogenesis.

5.1.3. Cardiac ^{13}C MRI—Cardiac metabolism exploits diverse mechanisms to maintain energy balance including metabolism of fatty acids, lactate, glucose, and ketone bodies. Changes in myocardial metabolism are therefore strongly associated with cardiac disease.

Author Manuscript Author Manuscript Author Manuscript Author Manuscript

As a result, MR imaging or spectroscopy of HP ^{13}C-labeled substrates is an attractive means of noninvasively measuring myocardial health. Observation of enzymatic conversion of injected HP [1-^{13}C] pyruvate to bicarbonate (Figure 7), lactate, and alanine [183], has been demonstrated in normal hearts and is sensitive to changes in ischemia-reperfusion models [184–187].

An alternative pyruvate probe, [2-^{13}C] pyruvate, allows for flux measurements of the tricarboxylic acid (TCA) cycle by detecting conversion of the secondary carbon to downstream TCA products such as lactate, acetylcarnitine, citrate, and glutamate [188, 189]. Combined approaches using both [1-^{13}C] and [2-^{13}C] pyruvate [190, 191] or dual-enriched [1,2-$^{13}C_2$] pyruvate allow for simultaneous investigation of pyruvate dehydrogenase flux, TCA cycle flux, and pH [192]. Other ^{13}C-labeled substrates applied to cardiac functional or metabolic imaging include [U-^{13}C] α-ketobutyrate [193], [1-^{13}C] lactic acid [194, 195], [1-^{13}C] acetate [196–199], ^{13}C urea [200], and [1-^{13}C] butyrate [201, 202]. Recently, co-polarization of ^{13}C urea and [1-^{13}C] pyruvate was demonstrated to simultaneously assess myocardial perfusion and metabolism [80].

5.2. Clinical research studies

HP ^{13}C MRSI in prostate cancer has advanced to phase I clinical trials. This transition has required several technological upgrades. SpinLab (General Electric, Niskayuna, New York, USA), a DNP system for clinical use, was introduced to support these translational studies by providing a sterile, disposable fluid path and quality control system, reducing the liquid helium consumption, and enabling simultaneous polarization of multiple ^{13}C samples [203]. To perform HP ^{13}C MRSI, clinical MRI scanners require dedicated multinuclear software and hardware including a broadband RF power amplifier, pre-amplifiers, and ^{13}C transmit and/or receive RF coils. However, the gradient hardware does not require any modifications to image heteronuclei aside from adjustment of the gradient amplitude to compensate for different gyromagnetic ratios. Logistically, the workflow for a HP ^{13}C study consists of hyperpolarizing the desired ^{13}C-labeled substrate in the clinical DNP system, dissoluting to physiologic pH, temperature, and osmolarity, performing quality control system checks to ensure sufficient filtration of unwanted gadolinium-chelates and electron paramagnetic agents, delivering the sample to the magnet room, and injecting the HP sample with concurrent data acquisition [204].

5.2.1. Prostate cancer phase trial—The first clinical trial for HP ^{13}C MRSI in prostate cancer was completed in 2013 at the University of California, San Francisco (NCT01229618) using [1-^{13}C] pyruvic acid as an indicator for altered glycolysis in prostate cancer patients [36]. This trial aimed to assess the safety and efficacy of injecting and imaging prostate cancer patients with HP [1-^{13}C] pyruvate. A total of 31 patients with untreated, biopsy-proven localized prostate cancer were enrolled in the trial. To address safety, a dose escalation scheme was established in which three ascending doses of [1-^{13}C] pyruvate were each delivered to 6 patients using a custom ^{13}C volume coil for transmission combined with a ^{1}H/^{13}C endorectal coil (Figure 8). Only mild adverse events were reported and no dose limiting toxicities were reached with the highest dose of HP [1-^{13}C] pyruvate being 0.43 mL/kg. Dynamic 2D and 3D data sets displayed increased lactate signal in

Author Manuscript Author Manuscript Author Manuscript Author Manuscript

tumors over normal tissues while single-time-point images were able to identify the presence, location, and size of cancer relative to surrounding normal prostate tissue [36]. While in most cases, the HP [1-^{13}C] lactate signal detection mimicked the cancer's location determined by ^{1}H MRI, some cases showed an interesting discrepancy between the ^{13}C signal and the ^{1}H multi-parametric MR imaging data (Figure 9).

5.2.2. New clinical research trials—Encouraged by this success, several other institutions are preparing for clinical trials utilizing HP [1-^{13}C] pyruvate, including the University of California, San Francisco (NCT02911467, NCT02526368, NCT02913131, and NCT02450201) and Sunnybrook Health Sciences Centre (NCT02647983 and NCT02844647). These trials have also extended beyond prostate cancer to include metabolic imaging of cardiac hypertension at Sunnybrook Health Sciences Centre (NCT02648009) and malignant solid tumors at Memorial Sloan Kettering (NCT02421380).

6. Applications of hyperpolarized gas MRI to pre-clinical and clinical research

6.1. Pre-clinical studies

Animal models of lung disease can provide useful test beds for establishing the feasibility and mechanism of functional measures derived from HP gas techniques. Several models have been developed to mimic specific disease processes, including radiation induced lung injury (RILI), elastase models of emphysema, bleomycin models of fibrotic lung injury, and allergic inflammation models of asthma. These models are useful as validation of non-invasive HP gas MRI methods compared to tissue histology. There is also an important role for assessing how disease patterns progress longitudinally and evaluating the sensitivity of HP gas MRI methods to such changes in a more controlled setting. Several studies have exploited these advantages in the disease models that follow.

6.1.1. Radiation induced lung injury (RILI)—RILI has long been a challenge in radiation therapy treatment for lung cancer with little advance in our understanding of factors that contribute to severity in some patients but not in others [205]. Devices for precise, regional delivery of radiation [206] have enabled comparison of irradiated vs. untreated lung parenchyma. HP ^{129}Xe has shown promise with respect to the lung inflammation and fibrotic processes underlying RILI because of its solubility in tissues and blood. For example, several feasibility studies in rat models of RILI have shown increased tissue signal from dissolved phase ^{129}Xe, suggestive of wall thickening in radiation treated lung tissues vs. control regions [207, 208]. Consistent with this observation, others have used DWI on ^{129}Xe MRI to detect reduced ADC values in control vs. irradiated rat lungs [209].

Both HP ^{13}C and ^{129}Xe MRI may play a role in detecting acute inflammation and injury in RILI. Hypoxic stress induced by radiation injury may lead to upregulation of glycolytic metabolism, increasing HP [1-^{13}C] pyruvate-to-lactate conversion on ^{13}C MRI in irradiated vs. control lungs. Increase in the lactate-to-pyruvate ratio has been observed in the lungs as a response to whole thorax irradiation compared to control rats, consistent with a

Author Manuscript Author Manuscript Author Manuscript Author Manuscript

corresponding increase in macrophage count in lavage fluid from irradiated vs. control lungs [210]. As a proof of concept study, both HP ^{129}Xe and HP ^{13}C MRI were used to assess metabolism via the HP ^{13}C MRI lactate-to-pyruvate ratio in the context of lung parenchymal tissue thickening measured using HP ^{129}Xe MRI. Both metabolic and microstructural changes in response to inflammation were observed in a rat model of RILI vs. control rats [211]. The combination of HP ^{13}C pyruvate MRI and HP ^{129}Xe MRI could potentially allow the evaluation of metabolic components of inflammatory cell activation in the context of functional consequences of tissue remodeling. These studies may lead to clinical research directed at identifying patients most susceptible to RILI as well as to improve understanding of the timing of inflammation, injury, and corresponding functional changes during radiation therapy of lung cancer.

6.1.2. Fibrotic lung disease—The complexity of the fibrotic lung disease process is a particularly challenging problem not well addressed by existing diagnostic tools, including computed tomography (CT) imaging (the clinical standard for diagnosis and staging of this disease). An alternative method for identifying tissues at risk for disease progression is needed in order to better stage and triage patients eligible for emerging new therapies [212]. Initial efforts using HP ^{3}He MRI focused on the feasibility of measuring ventilation changes [213] to better detect early progression in fibrotic lung disease, but these efforts had limited success for several reasons. First, ventilation is secondary to the underlying process of fibrotic injury and therefore an indirect measure of severity; and second, few therapies were available to treat these patients beyond simply limiting environmental exposure.

In the interim, FDA-approved anti-fibrotic therapies (perfinidone and nitanib [214]) have become available as possible treatments, making early detection and identification of progressive disease a high priority. These therapeutic advances have proceeded in parallel with advances in HP ^{129}Xe MRI images of gas transfer into the tissues and blood (Figure 10). Global and regional measures of RBC-to-tissue ratio using HP ^{129}Xe in ILD and IPF are extremely promising in both pre-clinical models and clinical research. The hypothesis is that lower values of RBC-to-tissue ratio are indicative of greater tissue density in the absence of gas exchange into the blood. This hypothesis is supported by pre-clinical findings in unilateral bleomycin models where one lung is treated and the other is a control, showing reduced RBC-to-tissue ratio in treated vs. control lungs in concert with increased fibrotic injury on histology [149] and in whole lung bleomycin-treated vs. saline controls [215].

6.1.3. Elastase models of emphysema—Emphysema is a prominent component of COPD, and elastase rodent and rabbit models have served an important role in mimicking the emphysema process. Both HP ^{3}He and ^{129}Xe diffusion-weighted studies have been used to validate quantitative measures of lung microstructural dimensions in elastase-treated animal models. These studies have served a useful role in optimizing ^{129}Xe DWI [216, 217] via comparison with the more mature ^{3}He DWI. Similar studies have explored the anisotropy and dependence on delay time of dimensional measures derived from DWI for both ^{3}He [218] and ^{129}Xe [219].

Pre-clinical studies in mice and rats have been used to validate other changes in lung function resulting from emphysematous loss of parenchymal tissue. Studies of fractional

Author Manuscript Author Manuscript Author Manuscript Author Manuscript

ventilation show expected decreases in ventilation relative to controls in a rat elastase model [220], for example. More recently, a decrease in HP ^{129}Xe MRI dissolved phase signal was observed after elastase treatment, presumably due to loss of lung parenchymal tissue confirmed on histology [221].

6.1.4. Asthma models—Asthma is a complex disease that is difficult to model. The most common approaches use allergic inflammation rodent models, typically via sensitization and exposure to ovalbumin to stimulate airway hyperreactivity. Allergic inflammation models demonstrated ventilation defects and localized inflammation in response to segmental challenge with allergen insufflation [222] and aerosolized methacholine challenge using ^{3}He MRI [223]. Similar studies have been duplicated with ^{129}Xe MRI and have gone a step further by demonstrating resolution of ventilation defects in response to bronchodilator [224]. However, such models remain limited in their ability to mimic the full complexity of asthma.

6.1.5. Hyperpolarized ^{129}Xe hyper-CEST—An exciting emerging area of research is the use of HP ^{129}Xe nuclei as biosensor constituents, enabling highly sensitive detection of a range of biomarkers using chemical exchange saturation transfer (CEST) techniques, specifically hyper-CEST. This technique exploits the sensitivity of the nuclear ^{129}Xe spin to disruption of the ^{129}Xe electron cloud by the local chemical microenvironment, enabling distinction between dissolved and bound ^{129}Xe nuclei via chemical shift differences. By introducing both HP ^{129}Xe and a targeted supramolecular host molecule, such as cryptophane-A, it is possible to use hyper-CEST MRI to differentiate between the ^{129}Xe nuclei in solution (e.g. blood plasma) and those bound to the targeted host molecules, enabling visualization of the targeted biomarker and, potentially, targeted therapeutic agents.

The feasibility of imaging with HP ^{129}Xe biosensors using hyper-CEST MRI was first demonstrated using cryptophane-A host cages targeted to avidin-functionalized agarose beads [225]. The potential applications of the technique have expanded to include *in vitro* labeling of cells and cell lysates. Klippel *et al.* demonstrated the ability to discriminate between cells labeled with cryptophane-A ^{129}Xe hosts and unlabeled cells [226], highlighting the potential of HP ^{129}Xe hyper-CEST MRI for cell tracking. The ability to distinguish specific cell types based on their surface receptors has also been experimentally tested *in vitro* for cells expressing surface proteins such as cluster of differentiation 14 (CD14) [227], cells exhibiting metabolically labeled cell-surface glycans [228], and lymphoma cells targeted by specific DNA aptamers attached to MS2 viral capsids enclosing cryptophane-A host molecules [229].

The promise of HP ^{129}Xe hyper-CEST has spurred the development of a range of additional biosensors for a variety of potential *in vitro* and *in vivo* applications including, but not limited to, detection of cancer biomarkers (e.g., protease activity, integrin receptors, and carbonic anhydrase isoforms) [230], mapping of enzyme activity both through hyper-CEST and magnetization transfer techniques with HP ^{129}Xe [231], identification of gene expression using genetically encoded reporter gas vesicles [232], and assessment of blood brain barrier integrity via detection of human brain microvascular endothelial cells [233]. The development of bifunctional cryptophane-A host molecules with attached fluorophores

Author Manuscript Author Manuscript Author Manuscript Author Manuscript

for both HP ^{129}Xe MRI and optical imaging has also created a means for improved contrast agent characterization and utility through multimodal and multiscale imaging [234]. Furthermore, the range of chemical shifts (~300 ppm) exhibited by HP ^{129}Xe in different bound states creates the potential for tracking multiple biosensors simultaneously (i.e., "multiplexing") and has been successfully tested *in vitro* by Klippel *et al.* who generated bi-modal contrast for two differently labeled mammalian cell populations [230, 235].

6.1.6. Hyperpolarized ^{129}Xe brain perfusion methods—Another emerging technique is HP ^{129}Xe cerebral perfusion imaging. Following inhalation, HP ^{129}Xe diffuses into the blood and is carried through the circulatory system to various organs, including the brain [32]. The sufficiently long T_1 of dissolved HP ^{129}Xe allows the use of CSI and MRS techniques to evaluate the HP ^{129}Xe distribution in the brain, enabling perfusion and relaxation measurements *in vivo*. This technique has been used in more qualitative applications, such as by Zhou *et al.* who used HP ^{129}Xe to observe the ischemic core in rat models of stroke [236]. However, much of the preliminary work in HP ^{129}Xe perfusion imaging has explored the use of different pharmacokinetic models to measure T_1 in the brain [237, 238]. Imai *et al.* also developed a perfusion model which estimates a rate constant dependent on the cerebral blood flow, the partition coefficient of ^{129}Xe between tissue and blood, and the T_1 relaxation rate. This model was tested by acquiring dynamic data in a mouse model of epilepsy. Dynamic changes in the estimated time constant were hypothesized to correspond to physiologic changes in the brain following kainic acid treatment, inducing epilepsy in the mouse [239].

6.2. Clinical research studies

HP gas MRI has faced many of the same challenges for clinical translation that HP ^{13}C MRI is currently addressing. While the methods and equipment for polarization differ, both techniques rely on much of the same multinuclear MRI hardware and software previously discussed. Like ^{13}C MRI, HP gas imaging requires dedicated RF coils for signal transmission and reception due to the vastly different ^{3}He and ^{129}Xe gyromagnetic ratios from conventional ^{1}H imaging (Table 1). Example HP ^{3}He and HP ^{129}Xe coils used for clinical imaging are displayed in Figure 11. Additionally, dedicated systems for delivery of HP gas are required that minimize the interaction of the HP gases with O_2 during delivery, thereby sustaining a longer T_1 time and polarization of the HP gas for improved imaging results (Figure 12).

6.2.1. Radiation induced lung injury (RILI)—Functional images of ventilation provide a potential means of image-guided treatment planning and mitigation of damage to healthy lung while maintaining or increasing dose to the treatment volume [240–243]. Adverse responses to therapy, including RILI or pneumonitis [244], can also be monitored. The field is now poised to take advantage of recent feasibility studies in rodent models and translate these promising approaches to studies of RILI in patients. Identifying patients at risk for RILI during radiation therapy lung cancer treatment remains a critical unsolved problem [245].

Author Manuscript Author Manuscript Author Manuscript Author Manuscript

6.2.2. Interstitial lung disease (ILD)—Clinical research studies of pulmonary HP ^{129}Xe gas exchange by Qing *et al.* [30, 31] have demonstrated abnormal barrier tissue-to-gas and RBC-to-gas ratios in COPD and asthma using a multi-echo spectral imaging technique. Similar work by Kaushik, Marshall and colleagues explored the relation of reduced gas exchange in IPF and dissolved phase HP ^{129}Xe using gas transfer spectroscopy [150, 246]. Barrier tissue-to-gas and RBC-to-gas ratios are promising new candidates for image biomarkers of gas exchange, with the potential to act as surrogates for treatment assessment and outcomes in longitudinal studies. Specifically, gas exchange imaging with ^{129}Xe MRI shows promise for detection of gas diffusion block in IPF, a disease that is presently untreatable and for which conventional diagnostic imaging methods such as CT are insensitive [150].

6.2.3. Asthma and COPD studies—The vast majority of clinical research studies using HP gas MRI have been performed in asthma [117, 122, 129, 134, 135, 247, 248] and COPD [123, 167, 249]. Studies of COPD have shown that ADC correlates with pulmonary function [167, 250, 251], is highly reproducible [162], and is sensitive to subclinical disease [124–126, 252] and disease progression [164, 249]. A multi-institutional prospective study of COPD found that ADC was more predictive of COPD severity and more highly correlated to the diffusing capacity of the lungs for carbon monoxide than quantitative CT [121]. In a separate 2-year longitudinal study of subjects with mild to moderate COPD, both ADC and VDP increased in the absence of significant change in the forced expiration volume in one second, suggesting progression detected by imaging but not by conventional methods [249]. In mild to moderate COPD, the VDP in particular is associated with severe outcomes such as hospitalizations for exacerbations, an association that is also not observed using conventional measures, including CT [136]. This work suggests the potential use of HP gas MRI to identify patients most likely to have severe outcomes at an earlier stage of disease progression, which in turn could allow more aggressive treatment regime to be utilized in these higher-risk individuals [253].

The greatest impact of HP gas MRI in asthma has been as a clinical research tool to characterize asthma phenotypes and to demonstrate treatment outcomes for individual patients not responsive to conventional anti-inflammatory therapies. Regional ventilation heterogeneity revealed by HP ^{3}He MRI has changed the way in which clinicians and researchers view this disease. Relatively large cross-sectional and longitudinal studies [132, 134, 254] have revealed that up to half of ventilation defects persist in the same locations over time intervals of several days to a year [254]. The persistence of ventilation defects in these studies was independent of asthma severity and medication use, suggesting that persistent defects were refractory to therapy. Because defects are observed even in asymptomatic patients and involve both the central and peripheral airways, conventional assumptions that asthma is a predominantly small airways disease have been challenged [255–257]. VDP and ADC-related measures are also associated with differences in lung microstructure in asthma compared with controls [258] and also with asthma risk factors in adults [259, 260] and children [256, 261].

Author Manuscript Author Manuscript Author Manuscript Author Manuscript

Image guided interventions using HP ^{3}He MRI have also been assessed and show promise for evaluating the effects of stent placement in COPD [262–264], and smooth muscle ablation treatments in asthma [265, 266].

6.2.4. Pediatric lung disease—Radiation dose is of increasing concern for longitudinal studies using CT and is especially problematic in pediatric and young adult populations [267, 268]. There will be a growing role for HP gas MRI in assessing therapy response and disease progression in CF [133, 269–271] and pediatric lung diseases in general as this technology, and MRI as a whole, are actively extended to study childhood [256, 261, 272] and neonatal [272, 273] lung diseases.

7. Future work

Limitations of HP gas MRI is principally a problem of access to, and cost of, the technology. Although admired and valued, these HP gas MRI techniques have not been widely disseminated for these and other reasons. However, there have recently been significant commercial and research investments in hyperpolarization gas technologies with two commercial vendors providing high performance polarizers with improved ease of use and reduced materials costs.

For HP ^{13}C and ^{15}N MRI applications, prolonging the relaxation times (T_1 and T_2) and overall polarization of HP agents would greatly enhance the available signal throughout the duration of the MR experiment. The enhanced HP signal could be utilized for greater image SNR, improved spatial resolution, and improved/extended temporal resolution, thereby increasing potential for clinical translation.

7.1. Strategies for prolonging T_1 and T_2

Several chemical formulation strategies exist to prolong the relaxation times of DNP-specific HP agents. Full or partial deuteration of ^{13}C-enriched compounds can greatly lengthen their T_1 times [274]. The T_1 of U-^{13}C labeled glucose was improved nearly 10-fold [71] enabling *in vivo* imaging and detection of downstream metabolites [70]. Replacement of protons with deuterons prevents dipolar relaxations between ^{13}C and ^{1}H nuclei, thereby lengthening T_1 times.

Careful handling of the HP substrate during sample transfer is another strategy to prolonging or preserving the T_1 time. The T_1 times of many HP ^{13}C substrates quickly decrease at low ambient magnetic fields in addition to having shortened T_1 times at higher magnetic fields. A handheld electromagnetic carrier for collection and transfer of ^{13}C samples improved or maintained image SNR from HP [^{13}C] urea and [1-^{13}C] pyruvate following dissolution and sample transfer [275].

Similarly, T_2 times can also be improved by co-labeling HP agents with multiple polarizable nuclei, enabling longer acquisition times and more time-intensive encoding schemes within a single excitation. Longer ^{13}C T_2 times were observed in dual-enriched [^{13}C, $^{15}N_2$] urea compared to [^{13}C] urea enabling acquisition of high resolution ^{13}C MR images on the order

Author Manuscript Author Manuscript Author Manuscript Author Manuscript

of ^{1}H MRI resolution (~1 mm) [276]. Similar enrichment schemes, while more costly, may enhance the available transverse signal.

7.2. Strategies for improving polarization

The limited availability of polarizer and multi-nuclear technology for HP ^{129}Xe and ^{3}He [277] in addition to high costs from limited global quantities of ^{3}He [25] necessitate migration to the more widely available ^{129}Xe nucleus [26]. Advances in ^{129}Xe SEOP polarization and isotope enrichment begin to address the technical challenges with this migration [10, 278]. Enrichment of the ^{129}Xe isotope has enabled robust replication of the major types of contrast-weighting demonstrated for ^{3}He MRI [27, 28]. Moreover, improved polarization methods for ^{129}Xe [10, 279] may make imaging of natural abundance HP ^{129}Xe feasible [280], thereby significantly reducing cost. Lastly, a recently introduced open source ^{129}Xe polarizer system offers a means to improve the availability of polarizer technology via local manufacturing using 3D printing technology [279, 281].

For DNP, increasing the overall maximum polarization of substrates can be achieved by several improvements in polarization techniques. Lanthanide doping of DNP samples is a well-established technique using trace amounts of free gadolinium (Gd^{3+}), holmium (Ho^{3+}), or gadolinium chelates to improve the nuclear polarization [282]. Gadolinium is an efficient relaxation agent due to its seven unpaired electrons and slow electronic relaxation rate and can substantially enhance solid-state polarization.

DNP efficiency could possibly be optimized by controlling polarization temperature and magnetic field strength. Comment and Merritt point out that reducing DNP temperatures below 1 K, where maximum ^{13}C polarization is predicted to be improved, will become technically challenging and expensive [40]. However, improvements have been shown at higher field strengths, with [1-^{13}C] pyruvate polarization increasing from 37% at 3.35 T [3] to 64% at 4.6 T [33]. At even higher field strengths (7 T), a maximal ^{13}C polarization was observed using nitroxyl radicals [283]. Furthermore, deuteration of the glassing solvent can improve maximum polarization by three-fold when used with free radical agents exhibiting large electron spin resonance linewidths (e.g., galvinoxyl, DPPH, and 4-oxo-TEMPO), at the expense of prolonged buildup times [284]. This deuteration effect is reversed in radical agents with small electron line resonance, such as BDPA and trityl OX063. Further, an excess electron concentration in the DNP polarizing solution can reduce the build-up time, but at the cost of lower maximum polarization overall [285].

8. Conclusions

The primary utility of functional imaging with HP agents is to visualize phenomena previously inaccessible or only poorly represented in clinical decision making. Examples of this range from high resolution patterns of ventilation and gas exchange heretofore only measured as whole lung averages, to regional dynamic metabolism in cancer and inflammation, which provide information more specific to metabolic pathways than existing fluorodeoxyglucose positron emission tomography methods. These approaches also open new opportunities to study the science of disease mechanisms that govern severity in lung

Author Manuscript Author Manuscript Author Manuscript Author Manuscript

disease and metastasis in cancer, with applications in asthma, COPD, CF, ILD, and renal and cardiac disease, as well as breast and prostate cancer.

Accelerating progress towards translation of these technologies is further supported by the significant commercial and research investments in hyperpolarization technologies. More than a dozen major research universities or institutes worldwide are now active in either HP gas or ^{13}C development. HP gases are more mature in their development than ^{13}C-based techniques, and are therefore better positioned for short-term clinical success. The translational potential of pulmonary MRI approaches has important advantages over established clinical methods such as pulmonary function tests and scintigraphy that could change the current cost-benefit calculus. Pulmonary function tests cannot easily characterize different phenotypes of disease. Furthermore, they represent a global assessment of the lungs that is generally insensitive to clinically important changes in disease severity that might impact patient management, especially as more therapy options become available and milder disease is targeted. The spatial resolution of scintigraphy is generally poorer than that achievable with MRI, and scintigraphy requires ionizing radiation. The use of X-ray based methods, including CT, diminish the numbers and types of imaging sessions that are practical for longitudinal assessment of chronic lung disease due to the potentially harmful effects of accumulated ionizing radiation exposure. The continued development of ultra-low dose CT [286] may impact this assessment, but it should also be noted that newer functional lung imaging methods using CT – for example, perfusion [287] and dual energy xenon CT [288] – require more radiation than standard chest CT. Moreover, recent advances in gradient performance and image reconstruction have significantly improved image quality for structural MRI of the lungs, leading to advances in combined structure-function assessment of disease severity and therapy response in CF that are only possible with pulmonary MRI [289].

There remain significant challenges to translating HP MRI methods to the clinic. HP ^{13}C, ^{15}N, and related liquid state agents require more technical development to increase the fraction and relaxation times of polarized nuclei. Further, all HP MRI methods require dedicated software, hardware, and trained personnel to conduct these advanced procedures. Despite these challenges, advances in sensitivity of diagnosis and treatment monitoring using metabolic imaging with agents such as HP [1-^{13}C] pyruvate have a clear pathway to translation for improving effectiveness of personalized treatments in cancer. Similarly, respiratory diseases still have significant unmet needs in terms of pharmaceutical development, minimally invasive interventions, longitudinal follow-up, and prognosis. Disorders such as asthma and COPD are widespread and will continue to be a leading cause of death and disease. The gas agents reviewed here underscore the unique ability of pulmonary MRI to measure the functional consequences of obstructive and restrictive lung diseases, while HP ^{13}C and ^{15}N substrates have the potential to offer unique, quantitative metabolic information for multiple organs and pathologies.

Acknowledgments

Funding:

1. U10 HL109168 (Jarjour)

Author Manuscript Author Manuscript Author Manuscript Author Manuscript

2. The Hartwell Foundation
3. Department of Medical Physics, School of Medicine and Public Health, UW-Madison
4. GE Healthcare
5. AAPM 2014 Graduate Fellowship
6. NIH awards UL1TR000427 and TL1TR000429

Acronyms

AA	ascorbic acid
ADC	apparent diffusion coefficient
CEST	chemical exchange saturation transfer
CF	cystic fibrosis
COPD	chronic obstructive pulmonary disease
CSI	chemical shift imaging
CT	computed tomography
DHA	dehydroascorbic acid
DNP	dynamic nuclear polarization
DWI	diffusion weighted imaging
EPI	echo-planar imaging
EPR	electron paramagnetic resonance
HP	hyperpolarized
IDEAL	iterative decomposition of water and fat with echo asymmetry and least-squares estimation
ILD	interstitial lung disease
IPF	idiopathic pulmonary fibrosis
LDH	lactate dehydrogenase
ME	metastability exchange
MRI	magnetic resonance imaging
MRSI	magnetic resonance spectroscopic imaging
NMR	nuclear magnetic resonance
PHIP	parahydrogen-induced polarization
PI3K	phosphatidylinositol-e-kinase

Author Manuscript Author Manuscript Author Manuscript Author Manuscript

pO_2	partial pressure of oxygen
RBC	red blood cell
redox	reduction/oxidation
RF	radio-frequency
RILI	radiation induced lung injury
SABRE	signal amplification by reversible exchange
SABRE-SHEATH	SABRE in shield enables alignment transfer to heteronuclei
SEOP	spin exchange optical pumping
SNR	signal-to-noise ratio
SPSP	spectral-spatial
TCA	tricarboxylic acid
TRAMP	transgenic adenocarcinoma of mouse prostate
VDP	ventilation defect percentage

References

1. Nikolaou P, Goodson BM, Chekmenev EY. NMR hyperpolarization techniques for biomedicine. Chemistry. 2015; 21(8):3156–66. [PubMed: 25470566]
2. Witte C, Schröder L. NMR of hyperpolarised probes. NMR in Biomedicine. 2013; 26(7):788–802. [PubMed: 23033215]
3. Ardenkjaer-Larsen JH, et al. Increase in signal-to-noise ratio of > 10,000 times in liquid-state NMR. Proc Natl Acad Sci U S A. 2003; 100(18):10158–63. [PubMed: 12930897]
4. Hovener JB, et al. PASADENA hyperpolarization of ^{13}C biomolecules: equipment design and installation. Magn Reson Mater Phy. 2009; 22(2):111–21.
5. Walker TG, Happer W. Spin-exchange optical pumping of noble-gas nuclei. Rev Mod Phys. 1997; 69(2):629–642.
6. Gentile TR, McKeown RD. Spin-polarizing ^{3}He nuclei with an arc-lamp-pumped neodymium-doped lanthanum magnesium hexaluminate laser. Phys Rev A. 1993; 47(1):456–467. [PubMed: 9908938]
7. Vander Heiden MG, Cantley LC, Thompson CB. Understanding the Warburg effect: the metabolic requirements of cell proliferation. Science. 2009; 324(5930):1029–33. [PubMed: 19460998]
8. van Beek EJ, et al. Functional MRI of the lung using hyperpolarized 3-helium gas. J Magn Reson Imaging. 2004; 20(4):540–54. [PubMed: 15390146]
9. Goodson BM, et al. In vivo NMR and MRI using injection delivery of laser-polarized xenon. Proc Natl Acad Sci U S A. 1997; 94(26):14725–9. [PubMed: 9405680]
10. Hersman FW, et al. Large production system for hyperpolarized ^{129}Xe for human lung imaging studies. Acad Radiol. 2008; 15(6):683–92. [PubMed: 18486005]
11. Kruger SJ, et al. Functional imaging of the lungs with gas agents. J Magn Reson Imaging. 2016; 43(2):295–315. [PubMed: 26218920]
12. Abragam A, Goldman M. Principles of dynamic nuclear polarisation. Rep Prog Phys. 1978; 41(3): 395–467.

Author Manuscript Author Manuscript Author Manuscript Author Manuscript

13. Atsarkin VA. Dynamic polarization of nuclei in solid dielectrics. Sov Phys Usp. 1978; 21(9):725–745.
14. Maly T, et al. Dynamic nuclear polarization at high magnetic fields. J Chem Phys. 2008; 128(5): 052211. [PubMed: 18266416]
15. Abragam A, Proctor W. A novel method of dynamic polarization of atomic nuclei in solids. Comptes Rendus. 1959; 246:2253.
16. Lumata L, et al. Impact of Gd^{3+} on DNP of [1-^{13}C]pyruvate doped with trityl OX063, BDPA, or 4-oxo-TEMPO. J Phys Chem A. 2012; 116(21):5129–38. [PubMed: 22571288]
17. Natterer J, Bargon J. Parahydrogen induced polarization. Prog Nucl Magn Reson Spectrosc. 1997; 31(4):293–315.
18. Duckett SB, Wood NJ. Parahydrogen-based NMR methods as a mechanistic probe in organic chemistry. Coord Chem Rev. 2008; 252:2278–2291.
19. Ross BD, et al. Hyperpolarized MR imaging: neurologic applications of hyperpolarized metabolism. AJNR Am J Neuroradiol. 2010; 31(1):24–33. [PubMed: 19875468]
20. Bhattacharya P, et al. Towards hyperpolarized ^{13}C-succinate imaging of brain cancer. J Magn Reson. 2007; 186(1):150–5. [PubMed: 17303454]
21. Hovener JB, et al. Quality assurance of PASADENA hyperpolarization for ^{13}C biomolecules. Magma. 2009; 22(2):123–34. [PubMed: 19067009]
22. Siddiqui S, et al. The use of hyperpolarized carbon-13 magnetic resonance for molecular imaging. Adv Drug Deliv Rev. 2016
23. Adams RW, et al. Reversible interactions with para-hydrogen enhance NMR sensitivity by polarization transfer. Science. 2009; 323(5922):1708–11. [PubMed: 19325111]
24. Theis T, et al. Direct and cost-efficient hyperpolarization of long-lived nuclear spin states on universal $^{15}N_2$-diazirine molecular tags. Sci Adv. 2016; 2(3):e1501438. [PubMed: 27051867]
25. Cho A. Physics. Helium-3 shortage could put freeze on low-temperature research. Science. 2009; 326(5954):778–9. [PubMed: 19892947]
26. Woods JC. Mine the moon for ^{3}He MRI? Not yet. J Appl Physiol (1985). 2013; 114(6):705–6. [PubMed: 23329817]
27. Kirby M, Parraga G. Pulmonary functional imaging using hyperpolarized noble gas MRI: six years of start-up experience at a single site. Acad Radiol. 2013; 20(11):1344–56. [PubMed: 24119346]
28. Mugler JP 3rd, Altes TA. Hyperpolarized ^{129}Xe MRI of the human lung. J Magn Reson Imaging. 2013; 37(2):313–31. [PubMed: 23355432]
29. Kaushik SS, et al. Probing the regional distribution of pulmonary gas exchange through single-breath gas- and dissolved-phase ^{129}Xe MR imaging. J Appl Physiol (1985). 2013; 115(6):850–60. [PubMed: 23845983]
30. Qing K, et al. Assessment of lung function in asthma and COPD using hyperpolarized ^{129}Xe chemical shift saturation recovery spectroscopy and dissolved-phase MRI. NMR Biomed. 2014; 27(12):1490–501. [PubMed: 25146558]
31. Qing K, et al. Regional mapping of gas uptake by blood and tissue in the human lung using hyperpolarized xenon-129 MRI. J Magn Reson Imaging. 2014; 39(2):346–59. [PubMed: 23681559]
32. Rao M, et al. High resolution spectroscopy and chemical shift imaging of hyperpolarized ^{129}Xe dissolved in the human brain in vivo at 1.5 tesla. Magn Reson Med. 2016; 75(6):2227–34. [PubMed: 27080441]
33. Johannesson H, Macholl S, Ardenkjaer-Larsen JH. Dynamic Nuclear Polarization of [1-^{13}C]pyruvic acid at 4.6 tesla. J Magn Reson. 2009; 197(2):167–75. [PubMed: 19162518]
34. Rowland IJ, et al. Hyperpolarized 13carbon MR. Curr Pharm Biotechnol. 2010; 11(6):709–19. [PubMed: 20497107]
35. Golman K, in ‘t Zandt R, Thaning M. Real-time metabolic imaging. Proc Natl Acad Sci U S A. 2006; 103(30):11270–5. [PubMed: 16837573]
36. Nelson SJ, et al. Metabolic imaging of patients with prostate cancer using hyperpolarized [1-^{13}C]pyruvate. Sci Transl Med. 2013; 5(198):198ra108.

Author Manuscript Author Manuscript Author Manuscript Author Manuscript

37. Brindle KM. Imaging metabolism with hyperpolarized ^{13}C-labeled cell substrates. J Am Chem Soc. 2015; 137(20):6418–27. [PubMed: 25950268]
38. Brindle KM, et al. Tumor imaging using hyperpolarized ^{13}C magnetic resonance spectroscopy. Magn Reson Med. 2011; 66(2):505–19. [PubMed: 21661043]
39. Gutte H, et al. The use of dynamic nuclear polarization ^{13}C-pyruvate MRS in cancer. Am J Nucl Med Mol Imaging. 2015; 5(5):548–60. [PubMed: 26550544]
40. Comment A, Merritt ME. Hyperpolarized magnetic resonance as a sensitive detector of metabolic function. Biochemistry. 2014; 53(47):7333–57. [PubMed: 25369537]
41. Rider OJ, Tyler DJ. Clinical implications of cardiac hyperpolarized magnetic resonance imaging. J Cardiovasc Magn Reson. 2013; 15:93. [PubMed: 24103786]
42. Gallagher FA, et al. Production of hyperpolarized [1,4-$^{13}C_2$]malate from [1,4-$^{13}C_2$]fumarate is a marker of cell necrosis and treatment response in tumors. Proc Natl Acad Sci U S A. 2009; 106(47):19801–6. [PubMed: 19903889]
43. Bohndiek SE, et al. Detection of tumor response to a vascular disrupting agent by hyperpolarized ^{13}C magnetic resonance spectroscopy. Mol Cancer Ther. 2010; 9(12):3278–88. [PubMed: 21159611]
44. Bohndiek SE, et al. Hyperpolarized ^{13}C spectroscopy detects early changes in tumor vasculature and metabolism after VEGF neutralization. Cancer Res. 2012; 72(4):854–64. [PubMed: 22223844]
45. Mignion L, et al. Monitoring chemotherapeutic response by hyperpolarized ^{13}C-fumarate MRS and diffusion MRI. Cancer Res. 2014; 74(3):686–94. [PubMed: 24285723]
46. Clatworthy MR, et al. Magnetic resonance imaging with hyperpolarized [1,4-$^{13}C_2$]fumarate allows detection of early renal acute tubular necrosis. Proc Natl Acad Sci U S A. 2012; 109(33):13374–9. [PubMed: 22837393]
47. Reuter S, et al. Oxidative stress, inflammation, and cancer: how are they linked? Free Radic Biol Med. 2010; 49(11):1603–16. [PubMed: 20840865]
48. Keshari KR, et al. Noninvasive in vivo imaging of diabetes-induced renal oxidative stress and response to therapy using hyperpolarized ^{13}C dehydroascorbate magnetic resonance. Diabetes. 2015; 64(2):344–52. [PubMed: 25187363]
49. Deutsch JC. Spontaneous hydrolysis and dehydration of dehydroascorbic acid in aqueous solution. Anal Biochem. 1998; 260(2):223–9. [PubMed: 9657882]
50. Gallagher FA, Kettunen MI, Brindle KM. Imaging pH with hyperpolarized ^{13}C. NMR Biomed. 2011; 24(8):1006–15. [PubMed: 21812047]
51. Gallagher FA, et al. Magnetic resonance imaging of pH in vivo using hyperpolarized ^{13}C-labelled bicarbonate. Nature. 2008; 453(7197):940–3. [PubMed: 18509335]
52. Gallagher FA, et al. Carbonic anhydrase activity monitored in vivo by hyperpolarized ^{13}C-magnetic resonance spectroscopy demonstrates its importance for pH regulation in tumors. Cancer Res. 2015; 75(19):4109–18. [PubMed: 26249175]
53. Ghosh RK, et al. Efficient production of hyperpolarized bicarbonate by chemical reaction on a DNP precursor to measure pH. Magn Reson Med. 2015; 74(5):1406–13. [PubMed: 25393101]
54. Schroeder MA, et al. Measuring intracellular pH in the heart using hyperpolarized carbon dioxide and bicarbonate: a ^{13}C and ^{31}P magnetic resonance spectroscopy study. Cardiovasc Res. 2010; 86(1):82–91. [PubMed: 20008827]
55. Flavell RR, et al. Application of Good's buffers to pH imaging using hyperpolarized ^{13}C MRI. Chem Commun (Camb). 2015; 51(74):14119–22. [PubMed: 26257040]
56. Jiang W, et al. Hyperpolarized ^{15}N-pyridine derivatives as pH-sensitive MRI agents. Sci Rep. 2015; 5:9104. [PubMed: 25774436]
57. Jindal AK, et al. Hyperpolarized ^{89}Y complexes as pH sensitive NMR probes. J Am Chem Soc. 2010; 132(6):1784–5. [PubMed: 20102196]
58. Keshari KR, Wilson DM. Chemistry and biochemistry of ^{13}C hyperpolarized magnetic resonance using dynamic nuclear polarization. Chem Soc Rev. 2014; 43(5):1627–59. [PubMed: 24363044]
59. Newbury NR, et al. Gaseous ^{3}He-^{3}He magnetic dipolar spin relaxation. Phys Rev A. 1993; 48(6): 4411–4420. [PubMed: 9910144]

Author Manuscript Author Manuscript Author Manuscript Author Manuscript

60. Repetto M, et al. Systematic T_1 improvement for hyperpolarized ^{129}xenon. J Magn Reson. 2015; 252:163–9. [PubMed: 25702572]
61. Thien F, et al. Feasibility of functional magnetic resonance lung imaging in Australia with long distance transport of hyperpolarized helium from Germany. Respirology. 2008; 13(4):599–602. [PubMed: 18494950]
62. Saam B, Happer W, Middleton H. Nuclear relaxation of ^{3}He in the presence of O_2. Phys Rev A. 1995; 52(1):862–865. [PubMed: 9912313]
63. Deninger AJ, et al. Quantification of regional intrapulmonary oxygen partial pressure evolution during apnea by ^{3}He MRI. J Magn Reson. 1999; 141(2):207–16. [PubMed: 10579944]
64. Li H, et al. Oxygen-dependent hyperpolarized ^{129}Xe brain MR. NMR Biomed. 2016; 29(3):220–5. [PubMed: 26915791]
65. Levy GC, Edlund U. Carbon-13 chemical shift anisotropy relaxation in organic compounds. J Am Chem Soc. 1975; 97(17):5031–5032.
66. Allerhand A, Doddrell D, Komoroski R. Natural abundance carbon-13 partially relaxed fourier transform nuclear magnetic resonance spectra of complex molecules. J Chem Phys. 1971; 55(1): 198–198.
67. Farrar TC, et al. Temperature-dependent carbon-13 relaxation studies of small molecules. J Am Chem Soc. 1972; 94(3):699–703.
68. Christensen CE, et al. Non-invasive in-cell determination of free cytosolic [NAD^+]/[NADH] ratios using hyperpolarized glucose show large variations in metabolic phenotypes. J Biol Chem. 2014; 289(4):2344–52. [PubMed: 24302737]
69. Harris T, Degani H, Frydman L. Hyperpolarized ^{13}C NMR studies of glucose metabolism in living breast cancer cell cultures. NMR Biomed. 2013; 26(12):1831–43. [PubMed: 24115045]
70. Rodrigues TB, et al. Magnetic resonance imaging of tumor glycolysis using hyperpolarized ^{13}C-labeled glucose. Nat Med. 2014; 20(1):93–7. [PubMed: 24317119]
71. Allouche-Arnon H, et al. In vivo magnetic resonance imaging of glucose - initial experience. Contrast Media Mol Imaging. 2013; 8(1):72–82. [PubMed: 23109395]
72. Stock KW, et al. Magnetic resonance T_2* measurements of the normal human lung in vivo with ultra-short echo times. Magn Reson Imaging. 1999; 17(7):997–1000. [PubMed: 10463650]
73. Chen XJ, et al. Spatially resolved measurements of hyperpolarized gas properties in the lung in vivo. Part II: T $*_2$. Magn Reson Med. 1999; 42(4):729–37. [PubMed: 10502762]
74. Wiesinger F, et al. IDEAL spiral CSI for dynamic metabolic MR imaging of hyperpolarized [1-^{13}C]pyruvate. Magn Reson Med. 2012; 68(1):8–16. [PubMed: 22127962]
75. Yen YF, et al. Apparent T_2 of ^{13}C-labeled Metabolites In Vivo. Proc Intl Soc Mag Reson Med. 2008; 16
76. Day SE, et al. Detecting tumor response to treatment using hyperpolarized ^{13}C magnetic resonance imaging and spectroscopy. Nat Med. 2007; 13(11):1382–7. [PubMed: 17965722]
77. MacDonald, AG. Physiological aspects of anaesthetics and inert gases. London: Academic Press Inc; 1978.
78. Koelsch BL, et al. Separation of extra- and intracellular metabolites using hyperpolarized ^{13}C diffusion weighted MR. J Magn Reson. 2016; 270:115–23. [PubMed: 27434780]
79. Miller GW, et al. A short-breath-hold technique for lung pO_2 mapping with ^{3}He MRI. Magn Reson Med. 2010; 63(1):127–36. [PubMed: 19918891]
80. Lau AZ, et al. Simultaneous assessment of cardiac metabolism and perfusion using copolarized [1-^{13}C]pyruvate and ^{13}C-urea. Magn Reson Med. 2016
81. Durst M, et al. Comparison of acquisition schemes for hyperpolarised ^{13}C imaging. NMR Biomed. 2015; 28(6):715–25. [PubMed: 25908233]
82. Wild JM, et al. Dynamic radial projection MRI of inhaled hyperpolarized ^{3}He gas. Magn Reson Med. 2003; 49(6):991–7. [PubMed: 12768575]
83. Chan HF, et al. Whole lung morphometry with 3D multiple b-value hyperpolarized gas MRI and compressed sensing. Magn Reson Med. 2016
84. Lee RF, et al. Advantages of parallel imaging in conjunction with hyperpolarized helium - a new approach to MRI of the lung. Magn Reson Med. 2006; 55(5):1132–41. [PubMed: 16586457]

Author Manuscript Author Manuscript Author Manuscript Author Manuscript

85. Cunningham CH, et al. Double spin-echo sequence for rapid spectroscopic imaging of hyperpolarized ^{13}C. J Magn Reson. 2007; 187(2):357–62. [PubMed: 17562376]
86. Cunningham CH, et al. Pulse sequence for dynamic volumetric imaging of hyperpolarized metabolic products. J Magn Reson. 2008; 193(1):139–46. [PubMed: 18424203]
87. Cunningham CH, et al. Frequency correction method for improved spatial correlation of hyperpolarized ^{13}C metabolites and anatomy. NMR Biomed. 2014; 27(2):212–8. [PubMed: 24353129]
88. Hu S, et al. 3D compressed sensing for highly accelerated hyperpolarized ^{13}C MRSI with in vivo applications to transgenic mouse models of cancer. Magn Reson Med. 2010; 63(2):312–21. [PubMed: 20017160]
89. Hu S, et al. Compressed sensing for resolution enhancement of hyperpolarized ^{13}C flyback 3D-MRSI. J Magn Reson. 2008; 192(2):258–64. [PubMed: 18367420]
90. Larson PE, et al. Fast dynamic 3D MR spectroscopic imaging with compressed sensing and multiband excitation pulses for hyperpolarized ^{13}C studies. Magn Reson Med. 2011; 65(3):610–9. [PubMed: 20939089]
91. Yen YF, et al. Imaging considerations for in vivo ^{13}C metabolic mapping using hyperpolarized ^{13}C-pyruvate. Magn Reson Med. 2009; 62(1):1–10. [PubMed: 19319902]
92. Mayer D, et al. Fast metabolic imaging of systems with sparse spectra: application for hyperpolarized ^{13}C imaging. Magn Reson Med. 2006; 56(4):932–7. [PubMed: 16941617]
93. Gordon JW, et al. Joint spatial-spectral reconstruction and k-t spirals for accelerated 2D spatial/1D spectral imaging of ^{13}C dynamics. Magn Reson Med. 2014; 71(4):1435–45. [PubMed: 23716402]
94. Adalsteinsson E, et al. Volumetric spectroscopic imaging with spiral-based k-space trajectories. Magn Reson Med. 1998; 39(6):889–98. [PubMed: 9621912]
95. Ramirez MS, et al. Radial spectroscopic MRI of hyperpolarized [1-^{13}C] pyruvate at 7 tesla. Magnetic Resonance in Medicine. 2014; 72(4):986–995. [PubMed: 24186845]
96. Jiang W, Lustig M, Larson PE. Concentric rings K-space trajectory for hyperpolarized ^{13}C MR spectroscopic imaging. Magn Reson Med. 2016; 75(1):19–31. [PubMed: 25533653]
97. Park I, et al. Evaluation of heterogeneous metabolic profile in an orthotopic human glioblastoma xenograft model using compressed sensing hyperpolarized 3D ^{13}C magnetic resonance spectroscopic imaging. Magn Reson Med. 2013; 70(1):33–9. [PubMed: 22851374]
98. Bernstein, MA., King, KF., Zhou, XJ. Handbook of MRI Pulse Sequences. Elsevier Academic Press; 2004.
99. Miller JJ, et al. Robust and high resolution hyperpolarized metabolic imaging of the rat heart at 7 t with 3d spectral-spatial EPI. Magn Reson Med. 2015
100. von Morze C, et al. Imaging of blood flow using hyperpolarized [^{13}C]urea in preclinical cancer models. J Magn Reson Imaging. 2011; 33(3):692–7. [PubMed: 21563254]
101. Leupold J, et al. Fast multiecho balanced SSFP metabolite mapping of ^{1}H and hyperpolarized ^{13}C compounds. Magma. 2009; 22(4):251–6. [PubMed: 19367422]
102. Block KT, Frahm J. Spiral imaging: a critical appraisal. J Magn Reson Imaging. 2005; 21(6):657–68. [PubMed: 15906329]
103. Tropp J, et al. Multi-channel metabolic imaging, with SENSE reconstruction, of hyperpolarized [1-^{13}C] pyruvate in a live rat at 3.0 tesla on a clinical MR scanner. J Magn Reson. 2011; 208(1): 171–7. [PubMed: 21130012]
104. Glover GH. Simple analytic spiral K-space algorithm. Magn Reson Med. 1999; 42(2):412–5. [PubMed: 10440968]
105. Brodsky EK, et al. Generalized k-space decomposition with chemical shift correction for non-Cartesian water-fat imaging. Magn Reson Med. 2008; 59(5):1151–64. [PubMed: 18429018]
106. Levin YS, et al. Optimization of fast spiral chemical shift imaging using least squares reconstruction: application for hyperpolarized ^{13}C metabolic imaging. Magn Reson Med. 2007; 58(2):245–52. [PubMed: 17654596]
107. Reeder SB, et al. Least-squares chemical shift separation for ^{13}C metabolic imaging. J Magn Reson Imaging. 2007; 26(4):1145–52. [PubMed: 17896366]

Author Manuscript Author Manuscript Author Manuscript Author Manuscript

108. Kaushik SS, et al. Single-breath clinical imaging of hyperpolarized ^{129}Xe in the airspaces, barrier, and red blood cells using an interleaved 3D radial 1-point Dixon acquisition. Magn Reson Med. 2016; 75(4):1434–43. [PubMed: 25980630]
109. Lau AZ, et al. Spectral-spatial excitation for rapid imaging of DNP compounds. NMR Biomed. 2011; 24(8):988–96. [PubMed: 21751271]
110. Schulte RF, Wiesinger F. Direct design of 2D RF pulses using matrix inversion. J Magn Reson. 2013; 235:115–20. [PubMed: 24013595]
111. Xing Y, et al. Optimal variable flip angle schemes for dynamic acquisition of exchanging hyperpolarized substrates. J Magn Reson. 2013; 234:75–81. [PubMed: 23845910]
112. Wang JX, et al. A general chemical shift decomposition method for hyperpolarized ^{13}C metabolite magnetic resonance imaging. Magn Reson Chem. 2016; 54(8):665–73. [PubMed: 27060361]
113. Meyer CH, et al. Simultaneous spatial and spectral selective excitation. Magn Reson Med. 1990; 15(2):287–304. [PubMed: 2392053]
114. Miller JJ, et al. Robust and high resolution hyperpolarized metabolic imaging of the rat heart at 7 T with 3D spectral-spatial EPI. Magn Reson Med. 2016; 75(4):1515–24. [PubMed: 25991606]
115. Maidens J, et al. Optimizing Flip Angles for Metabolic Rate Estimation in Hyperpolarized Carbon-13 MRI. IEEE Trans Med Imaging. 2016; 35(11):2403–2412. [PubMed: 27249825]
116. Larson PE, et al. Multiband excitation pulses for hyperpolarized ^{13}C dynamic chemical-shift imaging. J Magn Reson. 2008; 194(1):121–7. [PubMed: 18619875]
117. Fain SB, et al. Evaluation of structure-function relationships in asthma using multidetector CT and hyperpolarized He-3 MRI. Acad Radiol. 2008; 15(6):753–62. [PubMed: 18486011]
118. Sheikh K, et al. Pulmonary ventilation defects in older never-smokers. J Appl Physiol (1985). 2014; 117(3):297–306. [PubMed: 24903918]
119. Woodhouse N, et al. Combined helium-3/proton magnetic resonance imaging measurement of ventilated lung volumes in smokers compared to never-smokers. J Magn Reson Imaging. 2005; 21(4):365–9. [PubMed: 15779032]
120. Mathew L, et al. Hyperpolarized ^{3}He magnetic resonance imaging of chronic obstructive pulmonary disease: reproducibility at 3.0 tesla. Acad Radiol. 2008; 15(10):1298–311. [PubMed: 18790402]
121. van Beek EJ, et al. Hyperpolarised ^{3}He MRI versus HRCT in COPD and normal volunteers: PHIL trial. Eur Respir J. 2009; 34(6):1311–21. [PubMed: 19541712]
122. Tzeng YS, Lutchen K, Albert M. The difference in ventilation heterogeneity between asthmatic and healthy subjects quantified using hyperpolarized ^{3}He MRI. J Appl Physiol (1985). 2009; 106(3):813–22. [PubMed: 19023025]
123. Virgincar RS, et al. Quantitative analysis of hyperpolarized ^{129}Xe ventilation imaging in healthy volunteers and subjects with chronic obstructive pulmonary disease. NMR Biomed. 2013; 26(4): 424–35. [PubMed: 23065808]
124. Fain SB, et al. Early emphysematous changes in asymptomatic smokers: detection with ^{3}He MR imaging. Radiology. 2006; 239(3):875–83. [PubMed: 16714465]
125. Quirk JD, et al. In vivo detection of acinar microstructural changes in early emphysema with ^{3}He lung morphometry. Radiology. 2011; 260(3):866–74. [PubMed: 21734160]
126. Kirby M, et al. On the role of abnormal DL(CO) in ex-smokers without airflow limitation: symptoms, exercise capacity and hyperpolarised helium-3 MRI. Thorax. 2013; 68(8):752–9. [PubMed: 23604381]
127. Tustison NJ, et al. Ventilation-based segmentation of the lungs using hyperpolarized ^{3}He MRI. J Magn Reson Imaging. 2011; 34(4):831–41. [PubMed: 21837781]
128. Kirby M, et al. Hyperpolarized ^{3}He magnetic resonance functional imaging semiautomated segmentation. Acad Radiol. 2012; 19(2):141–52. [PubMed: 22104288]
129. Niles DJ, et al. Exercise-induced bronchoconstriction: reproducibility of hyperpolarized ^{3}He MR imaging. Radiology. 2013; 266(2):618–25. [PubMed: 23169798]
130. He M, et al. Extending semiautomatic ventilation defect analysis for hyperpolarized ^{129}Xe ventilation MRI. Acad Radiol. 2014; 21(12):1530–41. [PubMed: 25262951]

Author Manuscript Author Manuscript Author Manuscript Author Manuscript

131. Horn FC, et al. Lung ventilation volumetry with same-breath acquisition of hyperpolarized gas and proton MRI. NMR Biomed. 2014; 27(12):1461–7. [PubMed: 25208220]
132. de Lange EE, et al. Changes in regional airflow obstruction over time in the lungs of patients with asthma: evaluation with ^{3}He MR imaging. Radiology. 2009; 250(2):567–75. [PubMed: 19188325]
133. Kirby M, et al. Quantitative evaluation of hyperpolarized helium-3 magnetic resonance imaging of lung function variability in cystic fibrosis. Acad Radiol. 2011; 18(8):1006–13. [PubMed: 21536462]
134. de Lange EE, et al. Evaluation of asthma with hyperpolarized helium-3 MRI: correlation with clinical severity and spirometry. Chest. 2006; 130(4):1055–62. [PubMed: 17035438]
135. Kruger SJ, et al. Hyperpolarized Helium-3 MRI of exercise-induced bronchoconstriction during challenge and therapy. J Magn Reson Imaging. 2014; 39(5):1230–7. [PubMed: 24006239]
136. Kirby M, et al. Hyperpolarized ^{3}He ventilation defects used to predict pulmonary exacerbations in mild to moderate chronic obstructive pulmonary disease. Radiology. 2014; 273(3):887–96. [PubMed: 24960283]
137. Svenningsen S, et al. Hyperpolarized ^{3}He and ^{129}Xe MRI: differences in asthma before bronchodilation. J Magn Reson Imaging. 2013; 38(6):1521–30. [PubMed: 23589465]
138. Kirby M, et al. Pulmonary ventilation visualized using hyperpolarized helium-3 and xenon-129 magnetic resonance imaging: differences in COPD and relationship to emphysema. J Appl Physiol (1985). 2013; 114(6):707–15. [PubMed: 23239874]
139. Edelman RR, et al. Noninvasive assessment of regional ventilation in the human lung using oxygen-enhanced magnetic resonance imaging. Nat Med. 1996; 2(11):1236–9. [PubMed: 8898751]
140. Deninger AJ, et al. Assessment of a single-acquisition imaging sequence for oxygen-sensitive ^{3}He-MRI. Magn Reson Med. 2002; 47(1):105–14. [PubMed: 11754449]
141. Fischer MC, et al. Single-acquisition sequence for the measurement of oxygen partial pressure by hyperpolarized gas MRI. Magn Reson Med. 2004; 52(4):766–73. [PubMed: 15389934]
142. Rizi RR, et al. Determination of regional VA/Q by hyperpolarized ^{3}He MRI. Magn Reson Med. 2004; 52(1):65–72. [PubMed: 15236368]
143. Marshall H, et al. ^{3}He pO_2 mapping is limited by delayed-ventilation and diffusion in chronic obstructive pulmonary disease. Magn Reson Med. 2014; 71(3):1172–8. [PubMed: 23661570]
144. Hamedani H, et al. A variability study of regional alveolar oxygen tension measurement in humans using hyperpolarized ^{3}He MRI. Magn Reson Med. 2013; 70(6):1557–66. [PubMed: 23382040]
145. Hamedani H, et al. Alterations of regional alveolar oxygen tension in asymptomatic current smokers: assessment with hyperpolarized ^{3}He MR imaging. Radiology. 2015; 274(2):585–96. [PubMed: 25322340]
146. Wolber J, et al. Hyperpolarized ^{129}Xe NMR as a probe for blood oxygenation. Magn Reson Med. 2000; 43(4):491–6. [PubMed: 10748422]
147. Ruppert K, et al. Probing lung physiology with xenon polarization transfer contrast (XTC). Magn Reson Med. 2000; 44(3):349–57. [PubMed: 10975884]
148. Chang YV. MOXE: a model of gas exchange for hyperpolarized ^{129}Xe magnetic resonance of the lung. Magn Reson Med. 2013; 69(3):884–90. [PubMed: 22565296]
149. Driehuys B, et al. Imaging alveolar-capillary gas transfer using hyperpolarized ^{129}Xe MRI. Proc Natl Acad Sci U S A. 2006; 103(48):18278–83. [PubMed: 17101964]
150. Kaushik SS, et al. Measuring diffusion limitation with a perfusion-limited gas--hyperpolarized ^{129}Xe gas-transfer spectroscopy in patients with idiopathic pulmonary fibrosis. J Appl Physiol (1985). 2014; 117(6):577–85. [PubMed: 25038105]
151. Cleveland ZI, et al. Hyperpolarized Xe MR imaging of alveolar gas uptake in humans. PLoS One. 2010; 5(8):e12192. [PubMed: 20808950]
152. Dregely I, et al. Hyperpolarized Xenon-129 gas-exchange imaging of lung microstructure: first case studies in subjects with obstructive lung disease. J Magn Reson Imaging. 2011; 33(5):1052–62. [PubMed: 21509861]

Author Manuscript Author Manuscript Author Manuscript Author Manuscript

153. Patz S, et al. Human pulmonary imaging and spectroscopy with hyperpolarized $_{129}$Xe at 0.2T. Acad Radiol. 2008; 15(6):713–27. [PubMed: 18486008]
154. Chang YV, et al. Quantification of human lung structure and physiology using hyperpolarized ^{129}Xe. Magn Reson Med. 2014; 71(1):339–44. [PubMed: 24155277]
155. Golman K, et al. Metabolic imaging by hyperpolarized ^{13}C magnetic resonance imaging for in vivo tumor diagnosis. Cancer Res. 2006; 66(22):10855–60. [PubMed: 17108122]
156. Hill DK, et al. Model free approach to kinetic analysis of real-time hyperpolarized ^{13}C magnetic resonance spectroscopy data. PLoS One. 2013; 8(9):e71996. [PubMed: 24023724]
157. Reineri F, et al. Assessing the transport rate of hyperpolarized pyruvate and lactate from the intra- to the extracellular space. NMR Biomed. 2016; 29(8):1022–7. [PubMed: 27271484]
158. Gordon JW, et al. Application of flow sensitive gradients for improved measures of metabolism using hyperpolarized ^{13}C MRI. Magn Reson Med. 2016; 75(3):1242–8. [PubMed: 25951611]
159. Bankson JA, et al. Kinetic Modeling and Constrained Reconstruction of Hyperpolarized [1-^{13}C]-Pyruvate Offers Improved Metabolic Imaging of Tumors. Cancer Res. 2015; 75(22):4708–17. [PubMed: 26420214]
160. Kettunen MI, et al. Spin echo measurements of the extravasation and tumor cell uptake of hyperpolarized [1-^{13}C]lactate and [1-^{13}C]pyruvate. Magnetic Resonance in Medicine. 2013; 70(5):1200–1209. [PubMed: 23280500]
161. Smith MR, et al. In vivo imaging and spectroscopy of dynamic metabolism using simultaneous ^{13}C and ^{1}H MRI. IEEE Trans Biomed Eng. 2012; 59(1):45–9. [PubMed: 21775254]
162. Diaz S, et al. Hyperpolarized ^{3}He apparent diffusion coefficient MRI of the lung: reproducibility and volume dependency in healthy volunteers and patients with emphysema. J Magn Reson Imaging. 2008; 27(4):763–70. [PubMed: 18344208]
163. Halaweish AF, et al. Effect of lung inflation level on hyperpolarized ^{3}He apparent diffusion coefficient measurements in never-smokers. Radiology. 2013; 268(2):572–80. [PubMed: 23592768]
164. Diaz S, et al. Progression of emphysema in a 12-month hyperpolarized ^{3}He-MRI study: lacunarity analysis provided a more sensitive measure than standard ADC analysis. Acad Radiol. 2009; 16(6):700–7. [PubMed: 19362025]
165. Kaushik SS, et al. Diffusion-weighted hyperpolarized ^{129}Xe MRI in healthy volunteers and subjects with chronic obstructive pulmonary disease. Magn Reson Med. 2011; 65(4):1154–65. [PubMed: 21413080]
166. Fain SB, et al. Detection of age-dependent changes in healthy adult lungs with diffusion-weighted ^{3}He MRI. Acad Radiol. 2005; 12(11):1385–93. [PubMed: 16253850]
167. Salerno M, et al. Emphysema: hyperpolarized helium 3 diffusion MR imaging of the lungs compared with spirometric indexes--initial experience. Radiology. 2002; 222(1):252–60. [PubMed: 11756734]
168. Kauczor HU, et al. Imaging of the lungs using ^{3}He MRI: preliminary clinical experience in 18 patients with and without lung disease. J Magn Reson Imaging. 1997; 7(3):538–43. [PubMed: 9170039]
169. Siegel RL, Miller KD, Jemal A. Cancer statistics, 2016. CA Cancer J Clin. 2016; 66(1):7–30. [PubMed: 26742998]
170. Albers MJ, et al. Hyperpolarized ^{13}C Lactate, Pyruvate, and Alanine: Noninvasive Biomarkers for Prostate Cancer Detection and Grading. Cancer Res. 2008; 68(20):8607–8615. [PubMed: 18922937]
171. Chen AP, et al. Hyperpolarized C-13 spectroscopic imaging of the TRAMP mouse at 3T-initial experience. Magn Reson Med. 2007; 58(6):1099–106. [PubMed: 17969006]
172. Lupo JM, et al. Analysis of hyperpolarized dynamic ^{13}C lactate imaging in a transgenic mouse model of prostate cance. Magn Reson Imaging. 2011; 28(2):153–162.
173. Wilson DM, et al. Multi-compound Polarization by DNP Allows Simultaneous Assessment of Multiple Enzymatic Activities In Vivo. J Magn Reson. 2010; 205(1):141–147. [PubMed: 20478721]

Author Manuscript Author Manuscript Author Manuscript Author Manuscript

174. Keshari KR, et al. Hyperpolarized [1-^{13}C]Dehydroascorbate MR Spectroscopy in a Murine Model of Prostate Cancer: Comparison with ^{18}F-FDG PET. J Nucl Med. 2013; 54(6):922–928. [PubMed: 23575993]
175. Keshari KR, et al. Hyperpolarized [2-(13)C]-Fructose: A Hemiketal DNP Substrate for In Vivo Metabolic Imaging. J Am Chem Soc. 2009; 131(48):17591–6. [PubMed: 19860409]
176. Xu HN, et al. Is higher lactate an indicator of tumor metastatic risk? A pilot MRS study using hyperpolarized ^{13}C-pyruvate. Acad Radiol. 2014; 21(2):223–31. [PubMed: 24439336]
177. Xu HN, et al. In vivo metabolic evaluation of breast tumor mouse xenografts for predicting aggressiveness using the hyperpolarized ^{13}C-NMR technique. Adv Exp Med Biol. 2013; 789:237–42. [PubMed: 23852500]
178. Lau JY, et al. Voxel-by-voxel correlations of perfusion, substrate, and metabolite signals in dynamic hyperpolarized ^{13}C imaging. NMR Biomed. 2016; 29(8):1038–47. [PubMed: 27295304]
179. Harris T, et al. Kinetics of hyperpolarized $^{13}C_1$-pyruvate transport and metabolism in living human breast cancer cells. Proc Natl Acad Sci U S A. 2009; 106(43):18131–6. [PubMed: 19826085]
180. Lodi A, Woods SM, Ronen SM. Treatment with the MEK inhibitor U0126 induces decreased hyperpolarized pyruvate to lactate conversion in breast, but not prostate, cancer cells. NMR Biomed. 2013; 26(3):299–306. [PubMed: 22945392]
181. Ward CS, et al. Noninvasive detection of target modulation following phosphatidylinositol 3-kinase inhibition using hyperpolarized ^{13}C magnetic resonance spectroscopy. Cancer Res. 2010; 70(4):1296–305. [PubMed: 20145128]
182. Asghar Butt S, et al. Monitoring mammary tumor progression and effect of tamoxifen treatment in MMTV-PymT using MRI and magnetic resonance spectroscopy with hyperpolarized [1-^{13}C]pyruvate. Magn Reson Med. 2015; 73(1):51–8. [PubMed: 24435823]
183. Merritt ME, et al. Hyperpolarized ^{13}C allows a direct measure of flux through a single enzyme-catalyzed step by NMR. Proc Natl Acad Sci U S A. 2007; 104(50):19773–7. [PubMed: 18056642]
184. Golman K, et al. Cardiac metabolism measured noninvasively by hyperpolarized ^{13}C MRI. Magn Reson Med. 2008; 59(5):1005–13. [PubMed: 18429038]
185. Merritt ME, et al. Inhibition of carbohydrate oxidation during the first minute of reperfusion after brief ischemia: NMR detection of hyperpolarized $^{13}CO_2$ and $H^{13}CO_3$- Magn Reson Med. 2008; 60(5):1029–36. [PubMed: 18956454]
186. Schroeder MA, et al. In vivo assessment of pyruvate dehydrogenase flux in the heart using hyperpolarized carbon-13 magnetic resonance. Proc Natl Acad Sci U S A. 2008; 105(33):12051–6. [PubMed: 18689683]
187. Tyler DJ, et al. Application of Hyperpolarized Magnetic Resonance in the Study of Cardiac Metabolism. Appl Magn Reson. 2008; 34(3):523–531.
188. Schroeder MA, et al. Real-time assessment of Krebs cycle metabolism using hyperpolarized ^{13}C magnetic resonance spectroscopy. FASEB J. 2009; 23(8):2529–38. [PubMed: 19329759]
189. Atherton HJ, et al. Role of pyruvate dehydrogenase inhibition in the development of hypertrophy in the hyperthyroid rat heart: a combined magnetic resonance imaging and hyperpolarized magnetic resonance spectroscopy study. Circulation. 2011; 123(22):2552–61. [PubMed: 21606392]
190. Dodd MS, et al. In vivo alterations in cardiac metabolism and function in the spontaneously hypertensive rat heart. Cardiovasc Res. 2012; 95(1):69–76. [PubMed: 22593200]
191. Josan S, et al. In vivo investigation of cardiac metabolism in the rat using MRS of hyperpolarized [1-^{13}C] and [2-^{13}C]pyruvate. NMR Biomed. 2013; 26(12):1680–7. [PubMed: 23904148]
192. Chen AP, et al. Simultaneous investigation of cardiac pyruvate dehydrogenase flux, Krebs cycle metabolism and pH, using hyperpolarized [1,2-$^{13}C_2$]pyruvate in vivo. NMR Biomed. 2012; 25(2):305–11. [PubMed: 21774012]
193. von Morze C, et al. Hyperpolarized [^{13}C]ketobutyrate, a molecular analog of pyruvate with modified specificity for LDH isoforms. Magn Reson Med. 2016; 75(5):1894–900. [PubMed: 26059096]

Author Manuscript Author Manuscript Author Manuscript Author Manuscript

194. Chen AP, et al. Using [1-^{13}C]lactic acid for hyperpolarized ^{13}C MR cardiac studies. Magn Reson Med. 2015; 73(6):2087–93. [PubMed: 25046652]

195. Mayer D, et al. Application of hyperpolarized [1-^{13}C]lactate for the in vivo investigation of cardiac metabolism. NMR Biomed. 2012; 25(10):1119–24. [PubMed: 22278751]

196. Koellisch U, et al. Metabolic imaging of hyperpolarized [1-^{13}C]acetate and [1-^{13}C]acetylcarnitine - investigation of the influence of dobutamine induced stress. Magn Reson Med. 2015; 74(4):1011–8. [PubMed: 25298189]

197. Flori A, et al. Real-time cardiac metabolism assessed with hyperpolarized [1-^{13}C]acetate in a large-animal model. Contrast Media Mol Imaging. 2015; 10(3):194–202. [PubMed: 25201079]

198. Koellisch U, et al. Metabolic imaging of hyperpolarized [1-(13) C]acetate and [1-(13) C]acetylcarnitine - investigation of the influence of dobutamine induced stress. Magn Reson Med. 2015; 74(4):1011–8. [PubMed: 25298189]

199. Flori A, et al. Real-time cardiac metabolism assessed with hyperpolarized [1-13C]acetate in a large-animal model. Contrast Media & Molecular Imaging. 2015; 10(3):194–202. [PubMed: 25201079]

200. Lau AZ, et al. Cardiac perfusion imaging using hyperpolarized ^{13}C urea using flow sensitizing gradients. Magn Reson Med. 2016; 75(4):1474–83. [PubMed: 25991580]

201. Bastiaansen JA, Merritt ME, Comment A. Real time measurement of myocardial substrate selection in vivo using hyperpolarized ^{13}C magnetic resonance. Journal of Cardiovascular Magnetic Resonance. 2015; 17(1):O15.

202. Ball DR, et al. Hyperpolarized butyrate: a metabolic probe of short chain fatty acid metabolism in the heart. Magn Reson Med. 2014; 71(5):1663–9. [PubMed: 23798473]

203. Ardenkjaer-Larsen JH, et al. Dynamic nuclear polarization polarizer for sterile use intent. NMR Biomed. 2011; 24(8):927–32. [PubMed: 21416540]

204. Nelson SJ, et al. Strategies for rapid in vivo ^{1}H and hyperpolarized ^{13}C MR spectroscopic imaging. J Magn Reson. 2013; 229:187–97. [PubMed: 23453759]

205. Rodrigues G, et al. Prediction of radiation pneumonitis by dose–volume histogram parameters in lung cancer—a systematic review. Radiotherapy and oncology. 2004; 71(2):127–138. [PubMed: 15110445]

206. Sharma S, et al. Advanced Small Animal Conformal Radiation Therapy Device. Technol Cancer Res Treat. 2016

207. Doganay O, et al. Quantification of regional early stage gas exchange changes using hyperpolarized ^{129}Xe MRI in a rat model of radiation-induced lung injury. Med Phys. 2016; 43(5):2410. [PubMed: 27147352]

208. Li H, et al. Quantitative evaluation of radiation-induced lung injury with hyperpolarized xenon magnetic resonance. Magn Reson Med. 2016; 76(2):408–16. [PubMed: 26400753]

209. Ouriadov A, et al. Early stage radiation-induced lung injury detected using hyperpolarized ^{129}Xe Morphometry: Proof-of-concept demonstration in a rat model. Magn Reson Med. 2016; 75(6): 2421–31. [PubMed: 26154889]

210. Thind K, et al. Detection of radiation-induced lung injury using hyperpolarized ^{13}C magnetic resonance spectroscopy and imaging. Magn Reson Med. 2013; 70(3):601–9. [PubMed: 23074042]

211. Santyr G, et al. Anatomical, functional and metabolic imaging of radiation-induced lung injury using hyperpolarized MRI. NMR Biomed. 2014; 27(12):1515–24. [PubMed: 25156928]

212. Hansell DM, et al. CT staging and monitoring of fibrotic interstitial lung diseases in clinical practice and treatment trials: a position paper from the Fleischner Society. Lancet Respir Med. 2015; 3(6):483–96. [PubMed: 25975761]

213. Stephen MJ, et al. Quantitative assessment of lung ventilation and microstructure in an animal model of idiopathic pulmonary fibrosis using hyperpolarized gas MRI. Acad Radiol. 2010; 17(11):1433–43. [PubMed: 20934126]

214. Karimi-Shah BA, Chowdhury BA. Forced vital capacity in idiopathic pulmonary fibrosis--FDA review of pirfenidone and nintedanib. N Engl J Med. 2015; 372(13):1189–91. [PubMed: 25806913]

Author Manuscript Author Manuscript Author Manuscript Author Manuscript

215. Cleveland ZI, et al. 3D MRI of impaired hyperpolarized ^{129}Xe uptake in a rat model of pulmonary fibrosis. NMR Biomed. 2014; 27(12):1502–14. [PubMed: 24816478]
216. Mata JF, et al. Evaluation of emphysema severity and progression in a rabbit model: comparison of hyperpolarized ^{3}He and ^{129}Xe diffusion MRI with lung morphometry. J Appl Physiol (1985). 2007; 102(3):1273–80. [PubMed: 17110518]
217. Ruan W, et al. Detection of the mild emphysema by quantification of lung respiratory airways with hyperpolarized xenon diffusion MRI. Journal of Magnetic Resonance Imaging. 2016
218. Xu X, et al. Mapping of ^{3}He apparent diffusion coefficient anisotropy at sub-millisecond diffusion times in an elastase-instilled rat model of emphysema. Magn Reson Med. 2012; 67(4): 1146–53. [PubMed: 22135238]
219. Boudreau M, Xu X, Santyr GE. Measurement of ^{129}Xe gas apparent diffusion coefficient anisotropy in an elastase-instilled rat model of emphysema. Magn Reson Med. 2013; 69(1):211–20. [PubMed: 22378050]
220. Spector ZZ, et al. Quantitative assessment of emphysema using hyperpolarized ^{3}He magnetic resonance imaging. Magn Reson Med. 2005; 53(6):1341–6. [PubMed: 15906306]
221. Iguchi S, et al. Direct imaging of hyperpolarized ^{129}Xe alveolar gas uptake in a mouse model of emphysema. Magn Reson Med. 2013; 70(1):207–15. [PubMed: 22887860]
222. Holmes JH, et al. Noninvasive mapping of regional response to segmental allergen challenge using magnetic resonance imaging and [F-18] fluorodeoxyglucose positron emission tomography. Magnetic resonance in medicine. 2005; 53(6):1243–1250. [PubMed: 15906295]
223. Thomas AC, et al. A robust protocol for regional evaluation of methacholine challenge in mouse models of allergic asthma using hyperpolarized ^{3}He MRI. NMR Biomed. 2009; 22(5):502–15. [PubMed: 19204996]
224. Lilburn DM, et al. Investigating lung responses with functional hyperpolarized xenon-129 MRI in an ex vivo rat model of asthma. Magn Reson Med. 2016; 76(4):1224–35. [PubMed: 26507239]
225. Schroder L, et al. Molecular imaging using a targeted magnetic resonance hyperpolarized biosensor. Science. 2006; 314(5798):446–9. [PubMed: 17053143]
226. Klippel S, et al. Cell tracking with caged xenon: using cryptophanes as MRI reporters upon cellular internalization. Angew Chem Int Ed Engl. 2014; 53(2):493–6. [PubMed: 24307424]
227. Rose HM, et al. Development of an antibody-based, modular biosensor for ^{129}Xe NMR molecular imaging of cells at nanomolar concentrations. Proc Natl Acad Sci U S A. 2014; 111(32):11697–702. [PubMed: 25071165]
228. Witte C, et al. Live-cell MRI with xenon hyper-CEST biosensors targeted to metabolically labeled cell-surface glycans. Angew Chem Int Ed Engl. 2015; 54(9):2806–10. [PubMed: 25676513]
229. Jeong K, et al. Targeted Molecular Imaging of Cancer Cells Using MS2-Based ^{129}Xe NMR. Bioconjug Chem. 2016; 27(8):1796–801. [PubMed: 27454679]
230. Wang Y I, Dmochowski J. An Expanded Palette of Xenon-129 NMR Biosensors. Acc Chem Res. 2016; 49(10):2179–2187. [PubMed: 27643815]
231. Schnurr M, et al. Supramolecular Assays for Mapping Enzyme Activity by Displacement-Triggered Change in Hyperpolarized ^{129}Xe Magnetization Transfer NMR Spectroscopy. Angew Chem Int Ed Engl. 2015; 54(45):13444–7. [PubMed: 26426128]
232. Shapiro MG, et al. Genetically encoded reporters for hyperpolarized xenon magnetic resonance imaging. Nat Chem. 2014; 6(7):629–34. [PubMed: 24950334]
233. Schnurr M, et al. Brain endothelial cell targeting via a peptide-functionalized liposomal carrier for xenon hyper-CEST MRI. Adv Healthc Mater. 2015; 4(1):40–5. [PubMed: 24985966]
234. Rossella F, et al. Design and Characterization of Two Bifunctional Cryptophane A-Based Host Molecules for Xenon Magnetic Resonance Imaging Applications. ChemPlusChem. 2014; 79(10): 1463–1471.
235. Klippel S, Freund C, Schroder L. Multichannel MRI labeling of mammalian cells by switchable nanocarriers for hyperpolarized xenon. Nano Lett. 2014; 14(10):5721–6. [PubMed: 25247378]
236. Zhou X, et al. MRI of stroke using hyperpolarized ^{129}Xe. NMR Biomed. 2011; 24(2):170–5. [PubMed: 20821723]

Author Manuscript Author Manuscript Author Manuscript Author Manuscript

237. Zhou X, et al. Reinvestigating hyperpolarized ^{129}Xe longitudinal relaxation time in the rat brain with noise considerations. NMR Biomed. 2008; 21(3):217–25. [PubMed: 17557274]

238. Kilian W, Seifert F, Rinneberg H. Dynamic NMR spectroscopy of hyperpolarized ^{129}Xe in human brain analyzed by an uptake model. Magn Reson Med. 2004; 51(4):843–7. [PubMed: 15065259]

239. Imai H, et al. Development of a fast method for quantitative measurement of hyperpolarized ^{129}Xe dynamics in mouse brain. NMR Biomed. 2012; 25(2):210–7. [PubMed: 21755553]

240. Ireland RH, et al. Feasibility of image registration and intensity-modulated radiotherapy planning with hyperpolarized helium-3 magnetic resonance imaging for non-small-cell lung cancer. Int J Radiat Oncol Biol Phys. 2007; 68(1):273–81. [PubMed: 17448880]

241. Ireland RH, et al. An image acquisition and registration strategy for the fusion of hyperpolarized helium-3 MRI and x-ray CT images of the lung. Phys Med Biol. 2008; 53(21):6055–63. [PubMed: 18843168]

242. Bates EL, et al. Functional image-based radiotherapy planning for non-small cell lung cancer: A simulation study. Radiother Oncol. 2009; 93(1):32–6. [PubMed: 19552978]

243. Hodge CW, et al. On the use of hyperpolarized helium MRI for conformal avoidance lung radiotherapy. Med Dosim. 2010; 35(4):297–303. [PubMed: 19944585]

244. Mathew L, et al. Detection of longitudinal lung structural and functional changes after diagnosis of radiation-induced lung injury using hyperpolarized ^{3}He magnetic resonance imaging. Med Phys. 2010; 37(1):22–31. [PubMed: 20175462]

245. Linda A, Trovo M, Bradley JD. Radiation injury of the lung after stereotactic body radiation therapy (SBRT) for lung cancer: a timeline and pattern of CT changes. Eur J Radiol. 2011; 79(1): 147–54. [PubMed: 19954913]

246. Marshall H, et al. Direct visualisation of collateral ventilation in COPD with hyperpolarised gas MRI. Thorax. 2012; 67(7):613–7. [PubMed: 22286930]

247. Altes TA, et al. Hyperpolarized ^{3}He MR lung ventilation imaging in asthmatics: preliminary findings. J Magn Reson Imaging. 2001; 13(3):378–84. [PubMed: 11241810]

248. Samee S, et al. Imaging the lungs in asthmatic patients by using hyperpolarized helium-3 magnetic resonance: assessment of response to methacholine and exercise challenge. J Allergy Clin Immunol. 2003; 111(6):1205–11. [PubMed: 12789218]

249. Kirby M, et al. Chronic obstructive pulmonary disease: longitudinal hyperpolarized ^{3}He MR imaging. Radiology. 2010; 256(1):280–9. [PubMed: 20574101]

250. Morbach AE, et al. Diffusion-weighted MRI of the lung with hyperpolarized helium-3: a study of reproducibility. J Magn Reson Imaging. 2005; 21(6):765–74. [PubMed: 15906344]

251. Diaz S, et al. Validity of apparent diffusion coefficient hyperpolarized ^{3}He-MRI using MSCT and pulmonary function tests as references. Eur J Radiol. 2009; 71(2):257–63. [PubMed: 18514455]

252. Wang C, et al. Lung injury induced by secondhand smoke exposure detected with hyperpolarized helium-3 diffusion MR. J Magn Reson Imaging. 2014; 39(1):77–84. [PubMed: 24123388]

253. Kirby M, et al. Hyperpolarized helium-3 magnetic resonance imaging of chronic obstructive pulmonary disease exacerbation. J Magn Reson Imaging. 2013; 37(5):1223–7. [PubMed: 23124806]

254. de Lange EE, et al. The variability of regional airflow obstruction within the lungs of patients with asthma: assessment with hyperpolarized helium-3 magnetic resonance imaging. J Allergy Clin Immunol. 2007; 119(5):1072–8. [PubMed: 17353032]

255. Castro M, et al. Lung imaging in asthmatic patients: the picture is clearer. J Allergy Clin Immunol. 2011; 128(3):467–78. [PubMed: 21636118]

256. Castro M, Woods J. Insights into pediatric asthma with hyperpolarized magnetic resonance imaging of the lung. J Allergy Clin Immunol. 2013; 131(2):377–8. [PubMed: 23374266]

257. Teague WG, Tustison NJ, Altes TA. Ventilation heterogeneity in asthma. J Asthma. 2014; 51(7): 677–84. [PubMed: 24823323]

258. Wang C, et al. Assessment of the lung microstructure in patients with asthma using hyperpolarized ^{3}He diffusion MRI at two time scales: comparison with healthy subjects and patients with COPD. J Magn Reson Imaging. 2008; 28(1):80–8. [PubMed: 18581381]

Author Manuscript Author Manuscript Author Manuscript Author Manuscript

259. Johansson MW, et al. Markers of vascular perturbation correlate with airway structural change in asthma. Am J Respir Crit Care Med. 2013; 188(2):167–78. [PubMed: 23855693]
260. Marozkina NV, et al. Phenotype of asthmatics with increased airway S-nitrosoglutathione reductase activity. Eur Respir J. 2015; 45(1):87–97. [PubMed: 25359343]
261. Cadman RV, et al. Pulmonary ^{3}He magnetic resonance imaging of childhood asthma. J Allergy Clin Immunol. 2013; 131(2):369–76. e1–5. [PubMed: 23246019]
262. Snell GI, et al. The potential for bronchoscopic lung volume reduction using bronchial prostheses: a pilot study. Chest. 2003; 124(3):1073–80. [PubMed: 12970040]
263. Mata J, et al. Characterization and detection of physiologic lung changes before and after placement of bronchial valves using hyperpolarized helium-3 MR imaging: preliminary study. Acad Radiol. 2011; 18(9):1195–9. [PubMed: 21536465]
264. Mathew L, et al. Hyperpolarized ^{3}He functional magnetic resonance imaging of bronchoscopic airway bypass in chronic obstructive pulmonary disease. Can Respir J. 2012; 19(1):41–3. [PubMed: 22332133]
265. Cox G, et al. Asthma control during the year after bronchial thermoplasty. N Engl J Med. 2007; 356(13):1327–37. [PubMed: 17392302]
266. Thomen RP, et al. Regional ventilation changes in severe asthma after bronchial thermoplasty with ^{3}He MR imaging and CT. Radiology. 2015; 274(1):250–9. [PubMed: 25144646]
267. Kuo W, et al. Monitoring cystic fibrosis lung disease by computed tomography. Radiation risk in perspective. Am J Respir Crit Care Med. 2014; 189(11):1328–36. [PubMed: 24697683]
268. de Jong PA, et al. Estimation of the radiation dose from CT in cystic fibrosis. Chest. 2008; 133(5): 1289–91. author reply 1290–1.
269. Liszewski MC, et al. Magnetic resonance imaging of pediatric lung parenchyma, airways, vasculature, ventilation, and perfusion: state of the art. Radiol Clin North Am. 2013; 51(4):555–82. [PubMed: 23830786]
270. Mentore K, et al. Hyperpolarized HHe 3 MRI of the lung in cystic fibrosis: assessment at baseline and after bronchodilator and airway clearance treatment. Acad Radiol. 2005; 12(11):1423–9. [PubMed: 16253854]
271. Paulin GA, et al. Differences in hyperpolarized ^{3}He ventilation imaging after 4 years in adults with cystic fibrosis. J Magn Reson Imaging. 2015; 41(6):1701–7. [PubMed: 25174316]
272. Hahn AD, et al. Pulmonary MRI of neonates in the intensive care unit using 3D ultrashort echo time and a small footprint MRI system. J Magn Reson Imaging. 2016
273. Walkup LL, et al. Quantitative Magnetic Resonance Imaging of Bronchopulmonary Dysplasia in the Neonatal Intensive Care Unit Environment. Am J Respir Crit Care Med. 2015; 192(10):1215–22. [PubMed: 26186608]
274. Allouche-Arnon H, et al. A hyperpolarized choline molecular probe for monitoring acetylcholine synthesis. Contrast Media Mol Imaging. 2011; 6(3):139–47. [PubMed: 21698772]
275. Shang H, et al. Handheld electromagnet carrier for transfer of hyperpolarized carbon-13 samples. Magn Reson Med. 2016; 75(2):917–22. [PubMed: 25765516]
276. Reed GD, et al. High resolution ^{13}C MRI with hyperpolarized urea: in vivo T_2 mapping and ^{15}N labeling effects. IEEE Trans Med Imaging. 2014; 33(2):362–71. [PubMed: 24235273]
277. Fain S, et al. Imaging of lung function using hyperpolarized helium-3 magnetic resonance imaging: Review of current and emerging translational methods and applications. J Magn Reson Imaging. 2010; 32(6):1398–408. [PubMed: 21105144]
278. Ruset IC, Ketel S, Hersman FW. Optical pumping system design for large production of hyperpolarized. Phys Rev Lett. 2006; 96(5):053002. [PubMed: 16486926]
279. Nikolaou P, et al. Near-unity nuclear polarization with an open-source ^{129}Xe hyperpolarizer for NMR and MRI. Proc Natl Acad Sci U S A. 2013; 110(35):14150–5. [PubMed: 23946420]
280. Stewart NJ, et al. Feasibility of human lung ventilation imaging using highly polarized naturally abundant xenon and optimized three-dimensional steady-state free precession. Magn Reson Med. 2015; 74(2):346–52. [PubMed: 25916276]
281. Nikolaou P, et al. A 3D-printed high power nuclear spin polarizer. J Am Chem Soc. 2014; 136(4): 1636–42. [PubMed: 24400919]

Author Manuscript Author Manuscript Author Manuscript Author Manuscript

282. Ardenkjaer-Larsen JH, Macholl S, Jóhannesson H. Dynamic Nuclear Polarization with Trityls at 1.2 K. Applied Magnetic Resonance. 2008; 34(3):509–522.
283. Cheng T, et al. Over 35% liquid-state ^{13}C polarization obtained via dissolution dynamic nuclear polarization at 7 T and 1 K using ubiquitous nitroxyl radicals. Phys Chem Chem Phys. 2013; 15(48):20819–22. [PubMed: 24217111]
284. Lumata L, Merritt ME, Kovacs Z. Influence of deuteration in the glassing matrix on ^{13}C dynamic nuclear polarization. Phys Chem Chem Phys. 2013; 15(19):7032–5. [PubMed: 23552448]
285. Wolber J, et al. Generating highly polarized nuclear spins in solution using dynamic nuclear polarization. Nuclear Instruments and Methods in Physics Research Section A: Accelerators, Spectrometers, Detectors and Associated Equipment. 2004; 526(1–2):173–181.
286. Yu H, et al. Ultra-low dose lung CT perfusion regularized by a previous scan. Acad Radiol. 2009; 16(3):363–73. [PubMed: 19201366]
287. Goo HW. Dual-energy lung perfusion and ventilation CT in children. Pediatr Radiol. 2013; 43(3): 298–307. [PubMed: 23417255]
288. Kim WW, et al. Xenon-enhanced dual-energy CT of patients with asthma: dynamic ventilation changes after methacholine and salbutamol inhalation. AJR Am J Roentgenol. 2012; 199(5):975–81. [PubMed: 23096168]
289. Wielputz MO, et al. Magnetic resonance imaging detects changes in structure and perfusion, and response to therapy in early cystic fibrosis lung disease. Am J Respir Crit Care Med. 2014; 189(8):956–65. [PubMed: 24564281]
290. Bohndiek SE, et al. Hyperpolarized [1-^{13}C]-ascorbic and dehydroascorbic acid: vitamin C as a probe for imaging redox status in vivo. J Am Chem Soc. 2011; 133(30):11795–801. [PubMed: 21692446]
291. Keshari KR, et al. Hyperpolarized ^{13}C dehydroascorbate as an endogenous redox sensor for in vivo metabolic imaging. Proc Natl Acad Sci U S A. 2011; 108(46):18606–11. [PubMed: 22042839]
292. Duwel S, et al. Multiparametric human hepatocellular carcinoma characterization and therapy response evaluation by hyperpolarized ^{13}C MRSI. NMR Biomed. 2016; 29(7):952–60. [PubMed: 27195474]
293. Mazuel L, et al. Intracerebral synthesis of glutamine from hyperpolarized glutamate. Magn Reson Med. 2016
294. Cabella C, et al. In vivo and in vitro liver cancer metabolism observed with hyperpolarized [5-^{13}C]glutamine. J Magn Reson. 2013; 232:45–52. [PubMed: 23689113]
295. Hu S, et al. Rapid sequential injections of hyperpolarized [1-^{13}C]pyruvate in vivo using a sub-kelvin, multi-sample DNP polarizer. Magn Reson Imaging. 2013; 31(4):490–6. [PubMed: 23107275]
296. Koelsch BL, et al. Rapid in vivo apparent diffusion coefficient mapping of hyperpolarized ^{13}C metabolites. Magn Reson Med. 2015; 74(3):622–33. [PubMed: 25213126]
297. Sogaard LV, et al. In vivo measurement of apparent diffusion coefficients of hyperpolarized ^{13}C-labeled metabolites. NMR Biomed. 2014; 27(5):561–9. [PubMed: 24664927]
298. Scholz DJ, et al. Parameterization of hyperpolarized ^{13}C-bicarbonate-dissolution dynamic nuclear polarization. Magma. 2015; 28(6):591–8. [PubMed: 26449715]
299. von Morze C, et al. Detection of localized changes in the metabolism of hyperpolarized gluconeogenic precursors ^{13}C-lactate and ^{13}C-pyruvate in kidney and liver. Magn Reson Med. 2016
300. Yen YF, et al. T_2 relaxation times of ^{13}C metabolites in a rat hepatocellular carcinoma model measured in vivo using ^{13}C-MRS of hyperpolarized [1-^{13}C]pyruvate. NMR Biomed. 2010; 23(4):414–23. [PubMed: 20175135]
301. von Morze C, et al. Monitoring urea transport in rat kidney in vivo using hyperpolarized ^{13}C magnetic resonance imaging. Am J Physiol Renal Physiol. 2012; 302(12):F1658–62. [PubMed: 22492940]
302. Gordon JW, et al. Mis-estimation and bias of hyperpolarized apparent diffusion coefficient measurements due to slice profile effects. Magn Reson Med. 2016

Author Manuscript Author Manuscript Author Manuscript Author Manuscript

303. Day IJ, et al. Applications of DNP-NMR for the measurement of heteronuclear T1 relaxation times. J Magn Reson. 2007; 187(2):216–24. [PubMed: 17521933]

304. Lau AZ, et al. Rapid multislice imaging of hyperpolarized ^{13}C pyruvate and bicarbonate in the heart. Magn Reson Med. 2010; 64(5):1323–31. [PubMed: 20574989]

305. Ebner L, et al. The role of hyperpolarized ^{129}xenon in MR imaging of pulmonary function. Eur J Radiol. 2016

Author Manuscript Author Manuscript Author Manuscript Author Manuscript

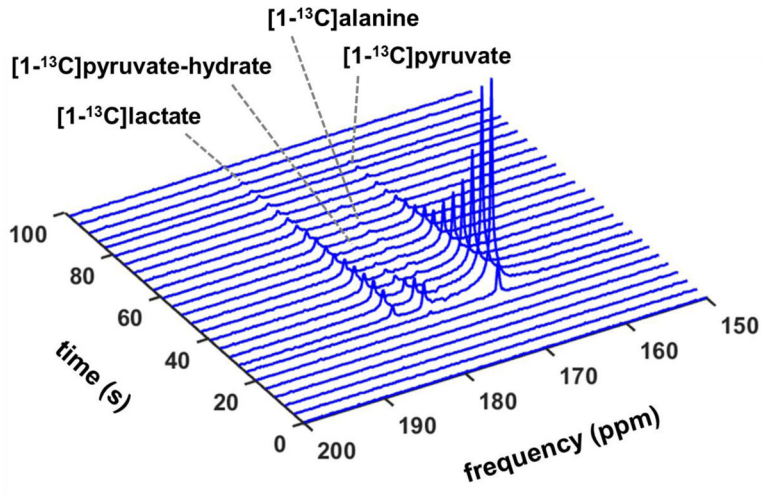

Figure 1.

Dynamic spectra displaying the transient decay of hyperpolarized metabolites in healthy normal rat kidneys. Time 20 s is the initiation of injection. The rate of decay for each species depends on the T_1 relaxation time, signal consumption by RF excitation, and rate of metabolic conversion.

Author Manuscript Author Manuscript Author Manuscript Author Manuscript

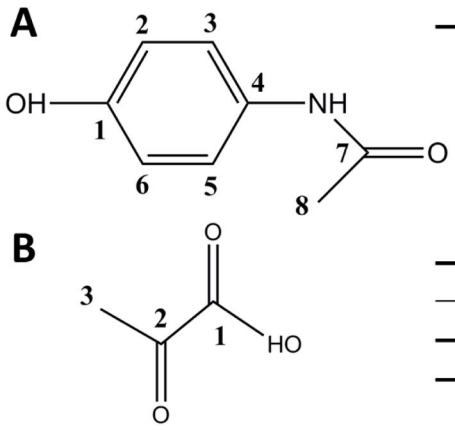

Atom	T_1 (s)
1	30
2,6	3
3,5	3
4	27
7	37
8	7

Atom	T_1 (s)
1	48

Figure 2.

Chemical structures and ^{13}C spin-lattice (T_1) relaxation times of acetaminophen (A) and [1-^{13}C] pyruvic acid (B) at 11.7 T. The placement of the ^{13}C atom in the carboxyl group of pyruvic acid results in a relatively long T_1. Acetaminophen has a variety of potential ^{13}C sites with T_1 values ranging from 3–37 s, with the shortest T_1 values for sites with increased dipolar coupling due to direct hydrogen bonds and the longest T_1 at the site with a carbonyl bond, reducing dipolar coupling [303].

Author Manuscript Author Manuscript Author Manuscript Author Manuscript

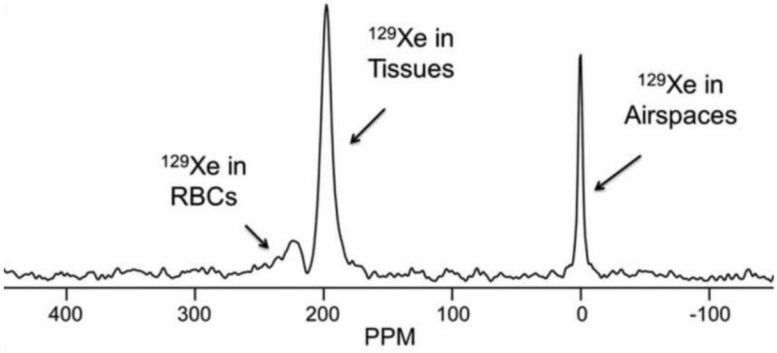

Figure 3.

MR spectrum detailing the gas phase and dissolved tissue and RBC phases of HP ^{129}Xe in the human lung. The ~200 ppm chemical shift between the gas and dissolved phases enables these different states to be visualized via spectral separation techniques. Note that for this spectrum, the gas phase peak was excited with a lower flip angle than the dissolved phases, reducing its magnitude by ~100 times (adapted from [11]).

Author Manuscript Author Manuscript Author Manuscript Author Manuscript

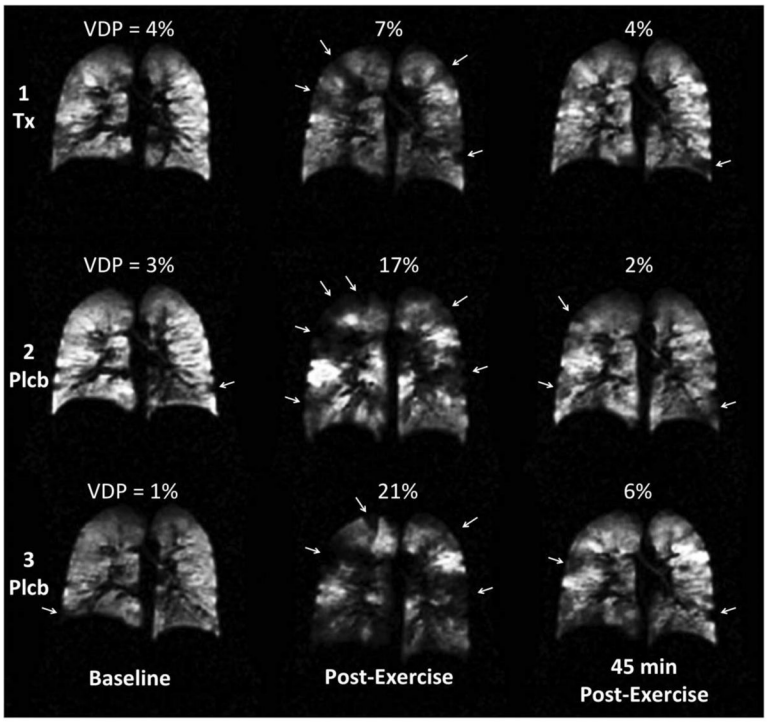

Figure 4.

Spin density images of HP ^{3}He gas distribution for a coronal slice in the lungs acquired pre-exercise (baseline) and at two time points post-exercise for a subject with exercise-induced bronchoconstriction and treatment with Montelukast. Images covering the lung volume were acquired for one treatment (Tx) visit and two placebo (Plcb) visits. White arrows indicate the ventilation defects visualized from these snapshots of the HP ^{3}He gas distribution, enabling calculation of the VDP. The VDP has the potential to act as a biomarker of exercise-induced bronchoconstriction as indicated by the higher VDPs in the post-exercise images (adapted from [11]).

Author Manuscript Author Manuscript Author Manuscript Author Manuscript

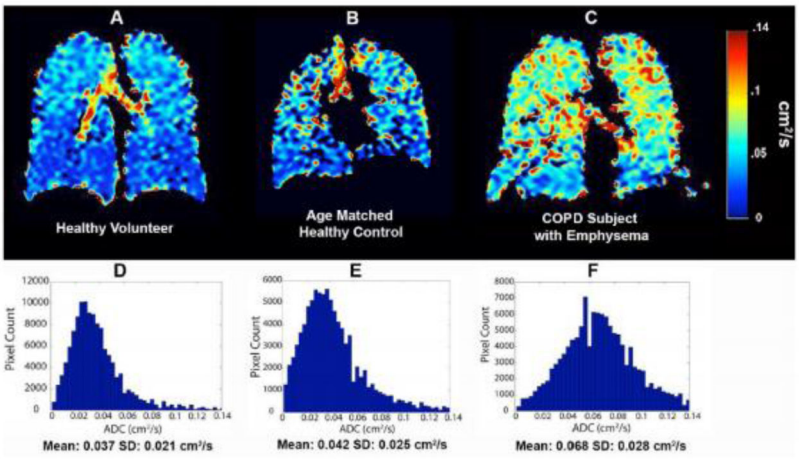

Figure 5.

Single-slice ^{129}Xe ADC maps and their corresponding whole-lung ADC histograms for a healthy volunteer (A, D), age matched healthy control (B, E), and COPD subject with emphysema (C, F). The lower ADC values in the healthy volunteer and age matched healthy control are indicative of normal alveolar microstructure while the higher ADC values in the airways indicate nearly free diffusion of the gas. The larger ADC values in parenchyma of the COPD subject with emphysema indicate alveolar destruction (adapted from [165]).

Author Manuscript Author Manuscript Author Manuscript Author Manuscript

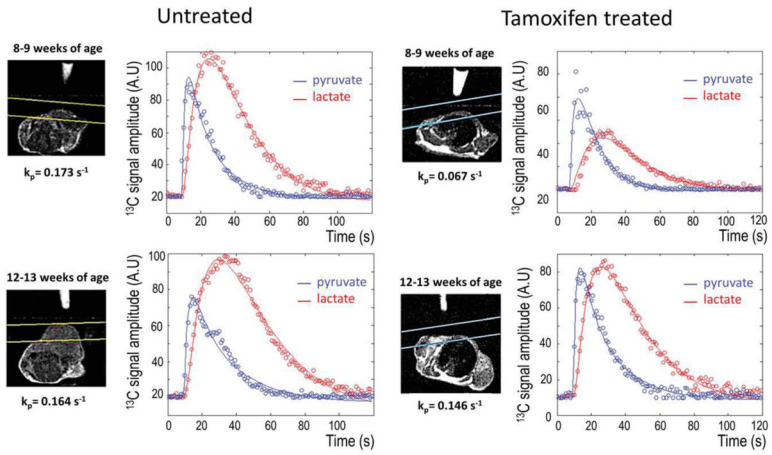

Figure 6.

^{1}H anatomical MR images depicting untreated (left) and tamoxifen-treated (right) MMTV-PymT breast cancer in mice at 8–9 weeks (first row) and 12–13 weeks (second row) of age. The slices used to acquire HP ^{13}C MRS are indicated by the paired lines on each ^{1}H anatomical image. The corresponding [1-^{13}C] pyruvate and [1-^{13}C] lactate dynamic time courses are given adjacent to each ^{1}H anatomical image, along with the calculated apparent conversion rate of pyruvate-to-lactate (k_p) (adapted from [182]).

Author Manuscript Author Manuscript Author Manuscript Author Manuscript

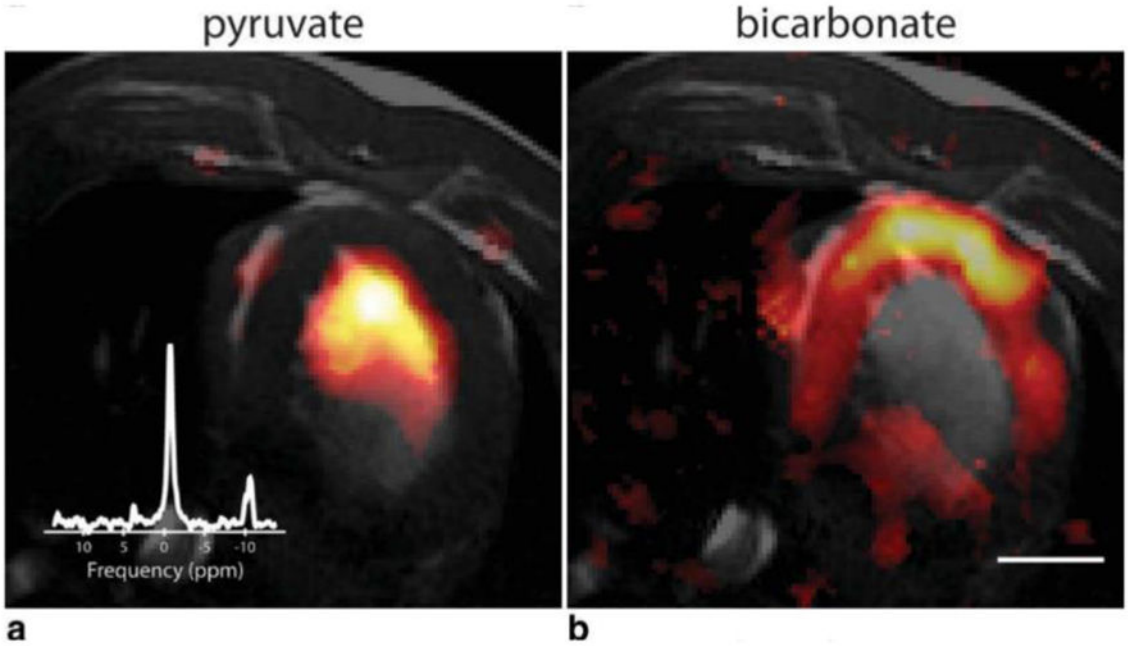

Figure 7.

HP [1-^{13}C] pyruvate (a) and ^{13}C bicarbonate (b) chemical shift images (color) in a 10 mm thick slice through the pig myocardium, overlaid on anatomical ^{1}H MR images (grayscale). The inset spectrum is the sum of the magnitude spectra from all voxels. The scale bar indicates 2 cm. This image was adapted from [304].

Author Manuscript Author Manuscript Author Manuscript Author Manuscript

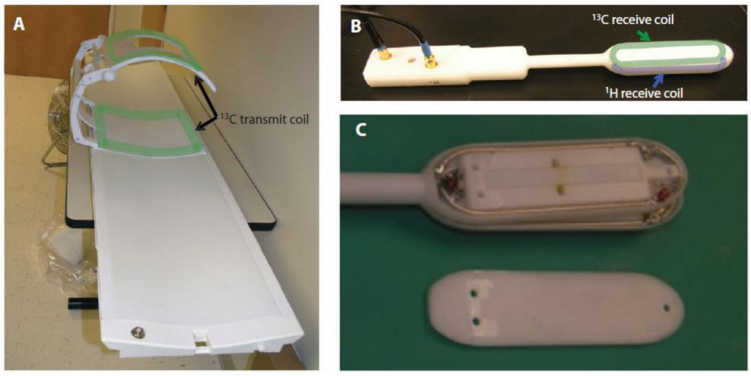

Figure 8.

^{13}C volume transmit coil (A) and dual-tuned ^{1}H/^{13}C endorectal coil (B) used in phase 1 trials for imaging the prostate cancer following a HP [1-^{13}C] pyruvate injection. The endorectal coil was 12 inches in length with 4 inches × 1 inch elements. The layered design of the endorectal coil is seen in (C). This image was adapted from [36].

Author Manuscript Author Manuscript Author Manuscript Author Manuscript

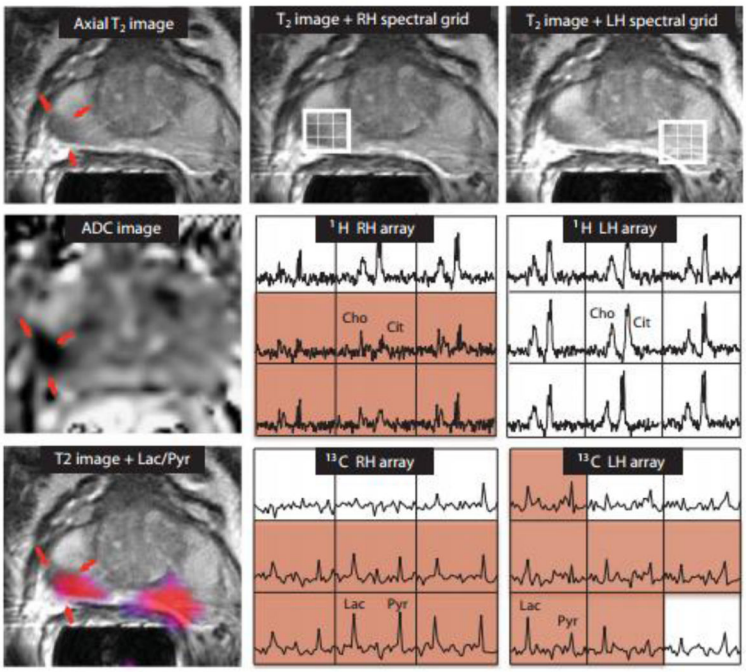

Figure 9.

MR images from a patient with bilateral biopsy-proven Gleason grade 3 + 3 prostate cancer. Both the axial T_2-weighted image and ADC image indicate decreased signal intensity (red arrows) in the suspected location of the right-hand (RH) lesion. However, the T_2-weighted and ADC images do not indicate a left-hand (LH) lesion. These results are corroborated by the RH and LH ^{1}H MRS results in which some spectra displayed reduced citrate and elevated choline/citrate (pink) on the right gland, but not left. The HP ^{13}C MRS arrays indicate elevated ratios of [1-^{13}C] lactate to [1-^{13}C] pyruvate (pink) on portions of both the right and left sides of the gland, indicative of upregulated glycolytic metabolism and consistent with the presence of prostate cancer. The ratio of lactate-to-pyruvate (color) is overlaid on the anatomical ^{1}H T_2-weighted reference image (grayscale) indicating agreement between the RH lesion identified by ^{1}H MRI and ^{13}C MRS, but not the LH lesion which was only indicated by ^{13}C MRS (adapted from [36]).

Author Manuscript Author Manuscript Author Manuscript Author Manuscript

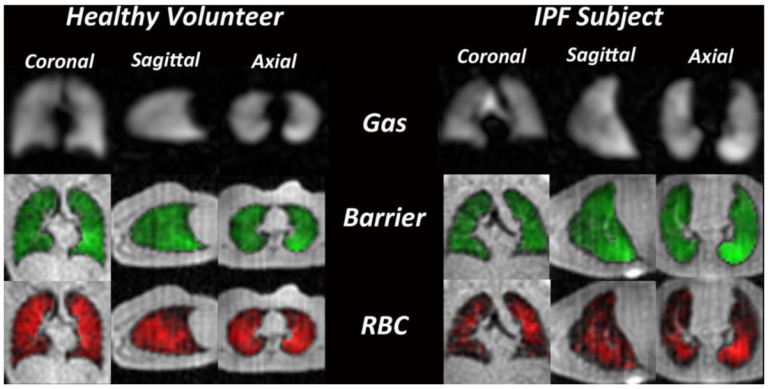

Figure 10.

Representative images of HP ^{129}Xe in the gas phase (grayscale), dissolved tissue phase (green) and dissolve RBC phase (red). For all phases, the ^{129}Xe signal was relatively homogeneously distributed in the healthy volunteer. Homogeneous gas and dissolved tissue distributions were also nearly homogeneous in the IPF subject. However, the RBC phase displayed significant heterogeneity indicating gas-transfer defects (adapted from [108]).

Author Manuscript Author Manuscript Author Manuscript Author Manuscript

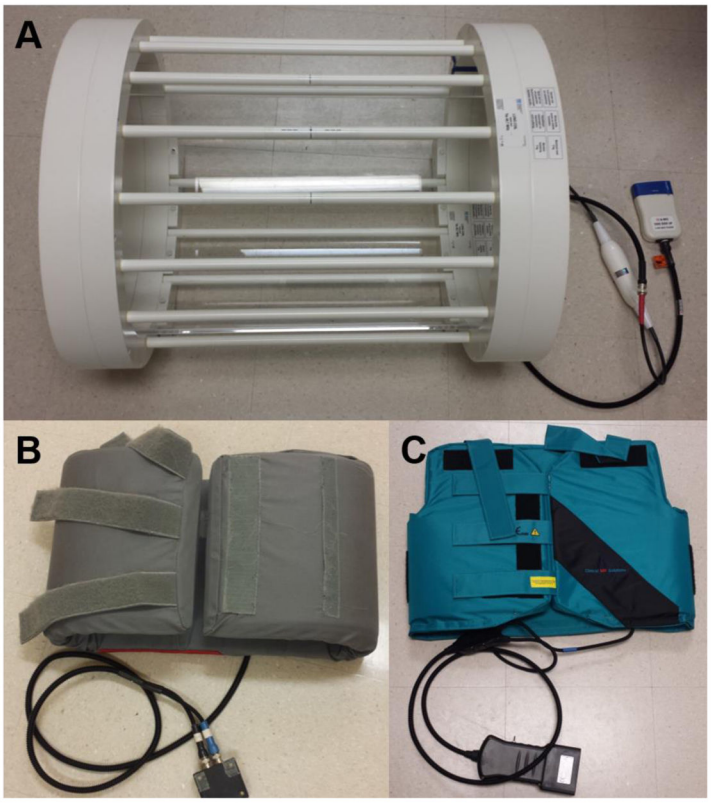

Figure 11.

Representative images of a HP ^{3}He receive birdcage coil (A), HP ^{3}He receive phased-array coil (B), and HP ^{129}Xe receive phased array coil (C), all used for pulmonary MR imaging. RF excitation is provided via the broadband capabilities of the MR system.

Author Manuscript Author Manuscript Author Manuscript Author Manuscript

Figure 12.

Components of a dedicated system for HP gas delivery to imaging subject (left) and view of the system in use (right). The bag containing HP gas is attached to the breathing apparatus just prior to inhalation and imaging. Unidirectional valves ensure inhaled gas is only drawn from the HP gas bag, while exhaled gas exits through flexible tubing and is vented outside of the scanner bore. Image adapted from [305].

Author Manuscript

Author Manuscript

Author Manuscript

Author Manuscript

Table 1

Physical properties of the most common HP gases [11]

	Hyperpolarized ^{3}He	Hyperpolarized ^{129}Xe
Gyromagnetic ratio (MHz/T)	33.434	11.777
Polarization	30–40%	8–40% [10]
T_1 at 1.5 T (s)	32	20
T_2 at 1.5 T (s)	2.00	0.31
T_2^* at 1.5 T (s)	0.020	0.019
Free diffusion coefficient (cm^2/s)	2.05	0.062
Apparent diffusion coefficient * (cm^2/s)	0.16	0.021
Gas density (g/cm^3)	1.34×10^{-4}	5.75×10^{-3}
Partition coefficient in blood (Ostwald – unitless)	0.0085	0.17

*within the restricted environment of the lung microstructure

Author Manuscript Author Manuscript Author Manuscript Author Manuscript

Table 2

Physical properties of common HP nuclei and substrates in metabolic MRS and MRSI

Nucleus	Gyromagnetic ratio (MHz/T)		Natural abundance (%)	
^{13}C	10.705 [98]		1.11 [58]	
^{15}N	−4.3156 [98]		0.37 [58]	
Substrate	**Reported LS polarizations**	**Apparent T_1 (s)**	**Apparent T_2 (s)**	**ADC ($\times 10^{-3}$ mm^2/s)**
[1-^{13}C] DHA	6–8% [290, 291]	56 (3 T), 21 (9.4 T), 21 (11.7 T) [58]	NR	NR
[2-^{13}C] fructose	12% [175]	13–15 (3 T), 16 (11.7 T) [58]	NR	NR
[1,4-$^{13}C_2$] fumaric acid	25–35% [38, 292]	70 (1 T) [292]; 24 (9.4 T), 29 (11.7 T) [58]	NR	NR
[U-^{2}H,U-^{13}C] glucose	13–19% [68–70]	12 (14.1 T) [58]; 14 (14.1 T) [68]; 10–14 (11.7 T) [69]; 9 (7 T) [70]; 10 (3 T) [71]	NR	NR
[1-^{13}C] glutamate	13–28% [38, 293]	30 (3 T) [293]; 26–34 (9.4 T) [58]	NR	NR
[5-^{13}C] glutamine	5–16% [38, 294]	25 (9.4 T) [58]; 20 (14.1 T) [294]	NR	NR
[1-^{13}C] pyruvic acid	up to 50% at 3.35 T [295]; up to 64% at 4.64 T [38]	67 (3 T), 48 (11.7 T), 44 (14.1 T) [58]; 63 (7 T) [95]	0.20–3.17 (RK), 0.22–4.71 (DP) [75]; 0.11–0.17 (MT) [160]	1.19–1.20 (EC), 0.10–0.17 (IC) [78]; 0.60 (RT), 0.71 (RBR) [296]; 1.1–1.5 (RM) [297]; 1.2–1.7 (MT) [160]
^{13}C bicarbonate	15% (Na) [38]; 19% (Cs) [298]	34–50 (Na, 3 T), 49 (Na, 11.7 T) [58]; 76–94 (Cs, 1 T), 53–62 (Cs, 3 T), 37–44 (Cs, 14 T) [298]	0.53–2.48 (RK), 0.13–1.22 (DP) [75]	NR
[1-^{13}C] sodium lactate	7–31% [38, 195, 299]	45–50.6 (3 T), 32–33.4 (14.1 T) [58]	0.35–2.80 (RK), 0.11–2.27 (DP) [75]; 0.52 (RL) [300]; 0.18–0.21 (MT) [160]	0.57–0.63 (EC), 0.17–0.19 (IC) [78]; 0.17 (RT), 0.44 (RBR) [296]; 0.4–0.7 (RM) [297]; 1.4–2.3 (MT) [160]
^{13}C urea	3–37% [38, 100, 276, 301]	44 (11.7 T), 35 (14.1 T) [58]; 46 (3 T) [276]	0.23 (RK), 0.28 (RBL) [276]	0.99 (ML) [302]

LS = liquid state, ADC = apparent diffusion coefficient, DHA = dehydroascorbic acid, NR = not reported, Na = sodium, Cs = cesium, DP = dog prostate, ML = murine liver, MT = murine tumor, RBL = rat blood, RBR = rat brain, RK = rat kidney, RL = rat liver, RM = rat muscle, RT = rat tumor, EC = extracellular, IC = intracellular